

Self-Attention for Raw Optical Satellite Time Series Classification

Marc Rußwurm and Marco Körner

*Chair of Remote Sensing Technology,
Department of Aerospace and Geodesy,
Technical University of Munich
Arcisstraße 21, 80333 Munich, Germany*

Abstract

The amount of available Earth observation data has increased dramatically in the recent years. Efficiently making use of the entire body information is a current challenge in remote sensing and demands for light-weight problem-agnostic models that do not require region- or problem-specific expert knowledge. End-to-end trained deep learning models can make use of raw sensory data by learning feature extraction and classification in one step solely from data. Still, many methods proposed in remote sensing research require implicit feature extraction through data preprocessing or explicit design of features.

In this work, we compare recent deep learning models on crop type classification on raw and preprocessed Sentinel 2 data. We concentrate on the common neural network architectures for time series, *i.e.*, 1D-convolutions, recurrence, a shallow random forest baseline, and focus on the novel self-attention architecture. Our central findings are that data preprocessing still increased the overall classification performance for all models while the choice of model was less crucial. Self-attention and recurrent neural networks, by their architecture, outperformed convolutional neural networks on raw satellite time series. We explore this by a feature importance analysis based on gradient back-propagation that exploits the differentiable nature of deep learning models. Further, we qualitatively show how self-attention scores focus selectively on few classification-relevant observations.

Keywords: Self-Attention, Transformer, Time Series Classification, Multitemporal Earth Observation, Crop Type Mapping, Vegetation Monitoring, Deep Learning

1. Introduction

Today, medium resolution Earth observation data is often provided free-of-charge since the Landsat program, jointly operated by the United States Geological Survey (USGS) and National Aeronautics and Space Administration (NASA), set a precedence by adopting an open data policy in 2008 [1; 2]. In recent years, the Copernicus program of the European Space Agency (ESA) joined this initiative by a growing family of Sentinel satellites that capture data from the Earth's surface at increasing temporal intervals. For instance, the Sentinel 2 multispectral satellites acquire data at up to 10 m resolution in 13 spectral bands every two to five days. Acquiring surface reflectance data at a high temporal frequency is a crucial tool for vegetation-related remote sensing applications, such as crop type mapping [3; 4], or forest monitoring [5; 6; 7]. This data-abundance, however, leads to computational and organizational challenges and demands for methods that are problem- and region-agnostic enough to utilize all available temporal data on large spatial scales. That these *challenges of Big Geo Data* are not solved yet can be seen on the low exploitation ratio of Sentinel 2 data in 2018. A large body of 7.76 TiB¹ Sentinel 2 data was published on a daily average. Still, only 7.6% of all published images in 2018² have been actually downloaded [8]. Accordingly, 12 out of 13 published images remained unused. Similar figures can be drawn for the Sentinel 1, 3, and 5 missions. This is a clear sign that, despite claims made by academia and industry, methods and principles of *big data analytics* are hardly applied to their full potential in the field of Earth observation. The reasons for this low exploitation ratio are manifold. First, visual

¹1 TiB = 2⁴⁰B

²62,317,329 published, 4,737,253 downloaded Sentinel 2 products in 2018

inspection of satellite images is still often the first step of data acquisition. Intermediate results are often required to be visually interpretable to allow for review by domain experts. Preprocessing steps, like atmospheric correction or manual or automatic cloud filtering, are common in remote sensing. All of these processes require computational resources or visual inspection that scales poorly when applying methods at dense temporal or global spatial scales. For instance, the commercial provider that preprocessed the datasets used in this work required multiple months to acquire, atmospherically correct, and organize the image time series for a comparatively small region of interest. In contrast, the raw Sentinel 2 time series were downloaded without active supervision within few days from Google Earth Engine. This demonstrates the demand for methods that utilize the entire body of available satellite data and, thus, requires minimal supervision by experts with region-specific expert knowledge. In principle, deep learning mechanisms seem well-suited to approximate preprocessing-like mechanisms by jointly learning feature extraction and classification within one neural network topology using gradient backpropagation. Developing models that do not strictly require extensive data preprocessing are likely a key contribution to utilize all available published satellite data accordingly in the future. In the scope of this objective, we assess three deep learning mechanisms on four deep learning models on selectively available preprocessed and readily available raw satellite data.

Summarizing, the contributions of this work are two-fold:

- i) We first present a large-scale evaluation of deep learning models on preprocessed and raw satellite data using three mechanisms—*i.e.*, convolution, recurrence, and self-attention—for crop type identification.
- ii) We further provide quantitative and qualitative analysis of self-attention in the context commonly used deep learning models for satellite time series classification.

2. Related Work

Since satellite data is inherently multi-temporal, this temporal dimension has been a topical focus for vegetation-related applications for a long time [4; 3]. The limited availability of multi-temporal satellite data and the excessive computational demand for temporal stacks of large-scale satellite images impeded broad exploitation of the temporal dimension. Methods relied on separate feature extraction, *i.e.*, calculation of vegetation indices [9; 10; 11; 12; 13] with temporal statistics [9; 12; 14], and classification mechanisms, *e.g.*, with Random Forest Classifiers [12; 15; 11] or Support Vector Machines [16; 17; 18], as summarized by [19; 20]. Similarly, the TimeSat software [21; 22] fits non-symmetric Gaussian curves to satellite time series. The parameters of these curves, *i.e.*, steepest ascent and descent, and their times of occurrence are assumed to coincide with key phenological characteristics, such as the onset of greenness or the date of senescence. This allows for detailed phenological analyses [23; 24] and can be used as distinctive feature for further classification [25; 26]. The *Continuous Change Detection and Classification (CCDC)* [27] first identifies “clear” observations by a prior cloud filtering with FMask [28; 29] on atmospherically corrected images. The FMask [28] algorithm itself is a functionally designed decision tree that exploits the physical properties of Landsat bands to identify cloud coverage and was later extended to more satellites [29]. The CCDC algorithm then explicitly models inter- and intra-annual seasonality by a sum of periodic functions for each pixel fitted with *Robust Iteratively Reweighted Least Squares (RIRLS)* [30; 31] to training data. The parameters of the periodic functions can be used as features for a subsequent classification. Similarly, the periodic functions can be used to predict future reluctance values and compared to measured data for change detection.

The *Breaks for Additive Seasonal and Trend (BFAST)* algorithm [32] similarly decomposes a satellite time series into piece-wise seasonal and linear components where the remainder can be used to detect anomalies and the periodicity can be used as feature for classification. The LandTrendr [33] aims at removing high-frequency components in a Landsat time series by finding a combination of successively simpler linear models, defined by vertices, that still explain the data sufficiently well. A variety of parameters can be adjusted to tune the model to specific regions and data through the number of allowed spikes (robustness to clouds), or number of segments (model complexity). These methods have been designed to require data preprocessing, *i.e.*, atmospheric correction or cloud filtering, some degree of direct supervision, *i.e.*, through the choice of parameters, or are tailored towards specific types of data, *e.g.*, Landsat for CCDC or MODIS for BFAST.

In contrast, Artificial Neural Networks [34; 35] aim at learning feature extraction and classification with a single dynamic model solely from the provided data with minimal supervision beyond the provided data. First success was achieved for the problem of the recognition of handwritten digits [36] using multi-layer neural networks trained with

gradient descent. However, comparatively recent advances in parallel processing and data availability [37; 38] were necessary to outperform common feature extraction and classification pipelines in computer vision [39; 40; 41; 42; 43] and natural language processing [44; 45; 46] on a large scale. Following these developments, mono-temporal Earth observation approaches have adapted 2D convolutional neural networks from the domain of computer vision with great success [47; 48; 49; 50]. Rotation-invariant feature extraction [51] for scene classification [52] and metric learning [53] has been similarly tested for remote sensing image classification. Methods from multi-temporal Earth observation [54; 55; 56; 57; 58; 59] adapted models from natural language processing. Here, recurrent neural networks [60], such as Long Short-Term Memory (LSTM) [61] or Gated Recurrent Units (GRU) [62], were commonly used in encode-decoder architectures [63] for generative prediction of words. In Earth observation, the encoder model was utilized for change detection [56; 57] and land cover [25], as well as for crop type identification [54; 59; 64; 65]. To utilize both spatial and temporal features from time series, combinations of convolutional layers and recurrent layers [58; 57] or convolutional-recurrent networks [66] have been explored and comprehensively compared [64]. These recurrent neural network encoders can be augmented by soft-attention mechanisms, originally developed for machine translation [67], as tested in [59]. Recently, the light-weight time-convolutional feed-forward neural networks have shown to be a powerful alternative [68] and have achieved promising results in crop type identification [69]. While the state-of-the-art in remote sensing remains focused on convolutional and recurrent architectures, *self-attention* [44], in combination with pre-training [45; 46], has started dominating the state-of-the-art in natural language processing. In the remote sensing context, self-attention has hardly been explored in the canon of existing work [70] on a comparative analysis with recurrence and convolutional mechanisms.

3. Method

In this section, we introduce the notation throughout this work and provide background on convolution, recurrence and address self-attention before employing these mechanisms in four neural network topologies in Section 4.

A deep learning model $f_{\Theta} : \mathcal{X} \mapsto \mathcal{Y}$ approximates a mapping from an input domain \mathcal{X} to a target domain \mathcal{Y} . These deep models are implemented by cascaded neural network layers that form a problem-agnostic, non-linear differentiable function. The parameters Θ are determined by minimizing an objective function $\mathcal{L}(\mathbf{y}, f_{\Theta}(\mathbf{X}))$ that quantifies the dissimilarity of ground truth labels $\mathbf{y} \in \mathcal{Y}$ and the model predictions $\hat{\mathbf{y}} = f_{\Theta}(\mathbf{X})$. This objective function is minimized iteratively via mini-batch stochastic gradient descent

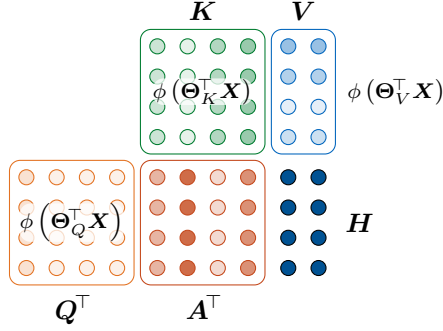
$$\Theta_{t+1} \leftarrow \Theta_t - \mu \mathbf{s}_t, \quad \text{with } \mathbf{s}_t = \frac{1}{N} \sum_{i=1}^N \frac{\partial}{\partial \Theta} \mathcal{L}(\mathbf{y}_i, f_{\Theta_t}(\mathbf{x}_i)) \quad . \quad (1)$$

The gradients $\frac{\partial}{\partial \Theta} \mathcal{L}$ are averaged over a batch of size N , while the learning rate μ determines the step size. This optimization scheme guarantees that the chosen parameters Θ are optimal for the observed dataset and objective function.

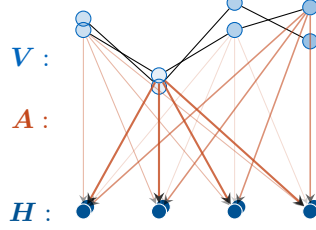
Deep learning for time series classification aims at learning the mapping $\hat{\mathbf{y}} = f_{\Theta}(\mathbf{X})$ from an input time series $\mathbf{X} \in \mathcal{X}^T = \mathbb{R}^{T \times D} = (\mathbf{x}_0, \mathbf{x}_1, \dots, \mathbf{x}_T)$ of individual measurements $\mathbf{x}_t \in \mathbb{R}^D$ of D features to one of C classes. These classes are represented by the *one-hot* target vector $\mathbf{y} \in \{0, 1\}^C$ where $y_i \in \{0, 1\}$ indicates the boolean class membership. We denote the approximation of the target vector as $\hat{\mathbf{y}} \in [0, 1]^C$. A neural network is a non-linear and differentiable function $f_{\Theta} = f_{\Theta_1}^{(1)} \circ f_{\Theta_2}^{(2)} \circ \dots \circ f_{\Theta_L}^{(L)}$ of L cascaded layers $f_{\Theta_l}^{(l)}$. Each layer $f_{\Theta_l}^{(l)} : \mathbf{H}^{(l)} \xrightarrow{\Theta_l} \mathbf{H}^{(l+1)}$ consists of a linear transformation Θ_l mapping an input representation $\mathbf{H}^l \in \mathbb{R}^{T \times D_h}$ to corresponding hidden features $\mathbf{H}^{l+1} \in \mathbb{R}^{T \times D_h}$ that encode increasingly higher-level features. In time series classification, one of the following mechanisms are used to implement this non-linear mapping.

3.1. Fully Connected Layers

A dense or fully connected layer $\mathbf{h}_t = f_{\Theta}^{\text{fc}}(\mathbf{x}_t) \in \mathbb{R}^{D_h}$ is applied independently at time instance t of a series. Each vector $\mathbf{x}_t \in \mathbb{R}^D$ is transformed into $\mathbf{h}_t = f_{\{\Theta_l, \Theta_b\}}^{\text{fc}}(\mathbf{x}_t) = \phi(\Theta_l^{\top} \mathbf{x}_t + \theta_b)$ by a linear transformation $\Theta_l \in \mathbb{R}^{D \times D_h}$ with optional bias translation $\theta_b \in \mathbb{R}^{D_h}$ followed by a non-linear activation function $\phi(\cdot) \in \{\tanh, \sigma, \text{ReLU}, \dots\}$.



(a) visualization of the matrix multiplications involved in the calculation of attention scores \mathbf{A}



(b) relationship between values and outputs drawn as bipartite graph

Figure 1: Schematic self-attention operation using $T_{\text{in}} = T_{\text{out}} = 4$, $D_{\text{in}} = D_{\text{out}} = 2$ and $D_{\text{h}} = 4$. The hidden output $\mathbf{H} \in \mathbb{R}^{4 \times 2}$ results from matrix multiplication with attention scores $\mathbf{A} \in [0, 1]^{4 \times 4}$ with a time series $\mathbf{V} \in \mathbb{R}^{4 \times 2}$. These attention scores themselves are calculated by a matrix multiplication between key $\mathbf{K} \in \mathbb{R}^{4 \times 4}$ and query matrices $\mathbf{Q} \in \mathbb{R}^{4 \times 4}$. In self-attention, all key, query and value matrices originate from an input time series \mathbf{X} transformed via a linear mapping $\mathbf{X}\Theta$ with a non-linear activation function $\phi(\cdot)$

3.2. Recurrent Layers

Recurrent Neural Networks [71] extend fully connected layers by contextual information from previous time steps $t - 1$. This results in a transformation $\mathbf{h}_t = f_{\Theta}^{\text{rnn}}(\mathbf{x}_t, \mathbf{h}_{t-1}) = \phi(\Theta_x^{\top} \mathbf{x}_t + \Theta_h^{\top} \mathbf{h}_{t-1} + \theta_b)$. This formulation is prone to *vanishing* and *exploding* gradients through time [61; 72; 60; 73] that inhibited the extraction of features from long-term temporal contexts. While the effect of exploding gradients could be controlled through gradient clipping, vanishing gradients have been addressed by the introduction of additional gates. This led to *Long Short-Term Memory (LSTM)* recurrent networks [61] that introduced four internal gates $\mathbf{f}_t = f_{\Theta_f}^{\text{rnn}}(\mathbf{x}_t, \mathbf{h}_{t-1})$, $\mathbf{i}_t = f_{\Theta_i}^{\text{rnn}}(\mathbf{x}_t, \mathbf{h}_{t-1})$, $\mathbf{g}_t = f_{\Theta_g}^{\text{rnn}}(\mathbf{x}_t, \mathbf{h}_{t-1})$, $\mathbf{o}_t = f_{\Theta_o}^{\text{rnn}}(\mathbf{x}_t, \mathbf{h}_{t-1})$. An additional *cell state* matrix \mathbf{c}_t was introduced as a container for the long-time temporal context. In each iteration, this cell state $\mathbf{c}_t = \mathbf{f}_t \odot \mathbf{c}_{t-1} + \mathbf{i}_t \odot \mathbf{g}_t$ is updated by element-wise multiplications \odot with the values of the forget, input, and modulation gates \mathbf{f}_t , \mathbf{i}_t , and \mathbf{g}_t , respectively. If the forget gate evaluates values close to zero, features in the prior cell state \mathbf{c}_{t-1} will be suppressed (forgotten). The modulation and input gates control the writing of new features from the input to the cell state \mathbf{c}_t . The cell output $\mathbf{h}_t = \mathbf{o}_t \odot \tanh(\mathbf{c}_t)$ is calculated using the result from the output gate \mathbf{o}_t and the new cell state \mathbf{c}_t . Overall, these transformations yield the long short-term memory update $f_{\Theta}^{\text{lstm}} : \mathbf{h}_t, \mathbf{c}_t \leftarrow \mathbf{x}_t, \mathbf{h}_{t-1}, \mathbf{c}_{t-1}$. An alternative to LSTMs are *Gated Recurrent Units (GRUs)* [62] that follow the same principle of additional gates, but are parameterized with fewer gates and less weights. Despite computational benefits, empirical evaluations did not show a significant difference in performance between these parameterizations [72].

3.3. 1D Convolutional Layers

Convolutional layers extract features by correlating the input signal $\mathbf{X} \in \mathbb{R}^{T \times D}$ with a set of D_{h} convolutional kernels $\Theta = (\Theta_0, \Theta_1, \dots, \Theta_{D_{\text{h}}})$ with $\Theta_d \in \mathbb{R}^{K \times D}$ employing a convolutional operation $\mathbf{H} = \phi(\mathbf{X} * \Theta)$ followed by an element-wise nonlinear activation function ϕ . The size of the convolutional kernel, K , determines the receptive field of each layer. In contrast to recurrent layers, convolutional layers extract features from a fixed temporal neighborhood. The receptive field increases through the number of layers. Convolutional layers perform well in the field of computer vision where features from a local neighborhood of an image are extracted with small local kernels. In a temporal context, larger kernel sizes are used. There, the learned kernel resembles a correlation between learned patterns in the time domain [74; 75] with recent applications in the field of remote sensing [69].

3.4. Self-Attention Layers

Attention mechanisms [67] allow a neural network to extract features from observations at specific time steps of an input time series of *values* $\mathbf{V} = (\mathbf{v}_0, \mathbf{v}_1, \dots, \mathbf{v}_{T_{\text{in}}}) \in \mathbb{R}^{T_{\text{in}} \times D_{\text{in}}}$. This is realized by a weighted sum $\mathbf{h}_i = \sum_{t=0}^{T_{\text{in}}} \alpha_t \mathbf{v}_t =$

$\alpha^\top \mathbf{V}$ of attention scores $\alpha \in [0, 1]^{T_{\text{in}}}$, $\sum_i \alpha_i = 1$. Extending this to a matrix multiplication

$$\mathbf{H} = \mathbf{A}^\top \mathbf{V} \quad (2)$$

with attention matrix $\mathbf{A} = (\mathbf{a}_0, \dots, \mathbf{a}_{T_{\text{out}}})$ and $\mathbf{H} = (\mathbf{h}_0, \dots, \mathbf{h}_{T_{\text{out}}}) \in \mathbb{R}^{T_{\text{out}} \times D_{\text{out}}}$, generates T_{out} output vectors in parallel. To illustrate these operations and to prepare for numerical results later in Section 8.4, we show a visual representation of these operations in Fig. 1. Attention scores themselves are the result of a second matrix multiplication $\mathbf{A} = \mathbf{Q}\mathbf{K}^\top$ in Eq. (3) of *key* and *query* matrices $\mathbf{K} \in \mathbb{R}^{T_{\text{in}} \times D_h}$ and $\mathbf{Q} \in \mathbb{R}^{T_{\text{out}} \times D_h}$, respectively. This results in the generic formulation of attention

$$\mathbf{H} = \underbrace{\text{softmax}(\mathbf{Q}\mathbf{K}^\top)}_{\mathbf{A}^\top} \mathbf{V} \quad (3)$$

that involves a softmax function to normalize \mathbf{A} . In self-attention [44]

$$\mathbf{H} = f_{\{\Theta_K, \Theta_Q, \Theta_V\}}(\mathbf{X}) = \text{softmax} \left(\frac{\phi(\Theta_Q^\top \mathbf{X}) \phi(\Theta_K^\top \mathbf{X})^\top}{\sqrt{D_h}} \right) \phi(\Theta_V^\top \mathbf{X}), \quad (4)$$

this formulation is adopted with unified dimensions $D_{\text{in}} = D_{\text{out}} = D_h$ and $T_{\text{in}} = T_{\text{out}}$ and where the keys $\mathbf{K} = \phi(\Theta_K^\top \mathbf{X})$, queries $\mathbf{Q} = \phi(\Theta_Q^\top \mathbf{X})$, and values $\mathbf{V} = \phi(\Theta_V^\top \mathbf{X})$ matrices originate from the same input matrix \mathbf{X} transformed by three linear transformations with non-linear activation function $\phi(\cdot)$. Following the original work [44], the attention scores are scaled by $\sqrt{D_h}$ for better gradient backpropagation. Today, such self-attention mechanisms are the core of state-of-the-art natural language processing models [45; 46] and will be experimentally analyzed later in Sections 8.4 and 8.6.

3.5. Soft-Attention

Soft-attention [76], as implemented in the DuPLO model [59], is a special case of Eq. (3) where values $\mathbf{V} = \mathbf{X}$ and queries $\mathbf{Q} = \tan(\Theta_Q \mathbf{X})$ are obtained from a linear transformation from the input tensor \mathbf{X} . In contrast to self-attention, the keys $\mathbf{K} = \Theta_K$ are realized by a fixed weight matrix which is learned by gradient descent. Following the definitions of [59] and modified from Eq. (4), soft-attention yields

$$\mathbf{h} = f_{\{\Theta_K, \Theta_A\}}(\mathbf{X}) = \underbrace{\text{softmax}(\tan(\Theta_A^\top \mathbf{X}) \Theta_K)^\top}_{\alpha^\top} \mathbf{X} \quad (5)$$

where the non-linearity ϕ is implemented as tangens \tan without scaling factor D_h . We compare self-attention with the simplified soft-attention in a dedicated experiment in Section 8.5.

4. Models

The previous section provided an overview on neural network layers used for temporal feature extraction and introduced temporal convolution, recurrence, and self-attention. In this section, we describe four neural network topologies, each of them using one of these layer mechanisms, which will be evaluated experimentally in the following³.

4.1. Recurrent Long Short-Term Memory Neural Network

We designed a multi-layer *Recurrent Neural Network (RNN)* [71] with *Long Short-Term Memory (LSTM)*[61] cell architecture, similar to our previous work [54]. This network encodes a satellite time series to increasingly higher-level D -dimensional representations through N cascaded bidirectional LSTM layers. The hidden states are initialized

³The models are available at <https://github.com/marccoru/crop-type-mapping/tree/master/src/models>

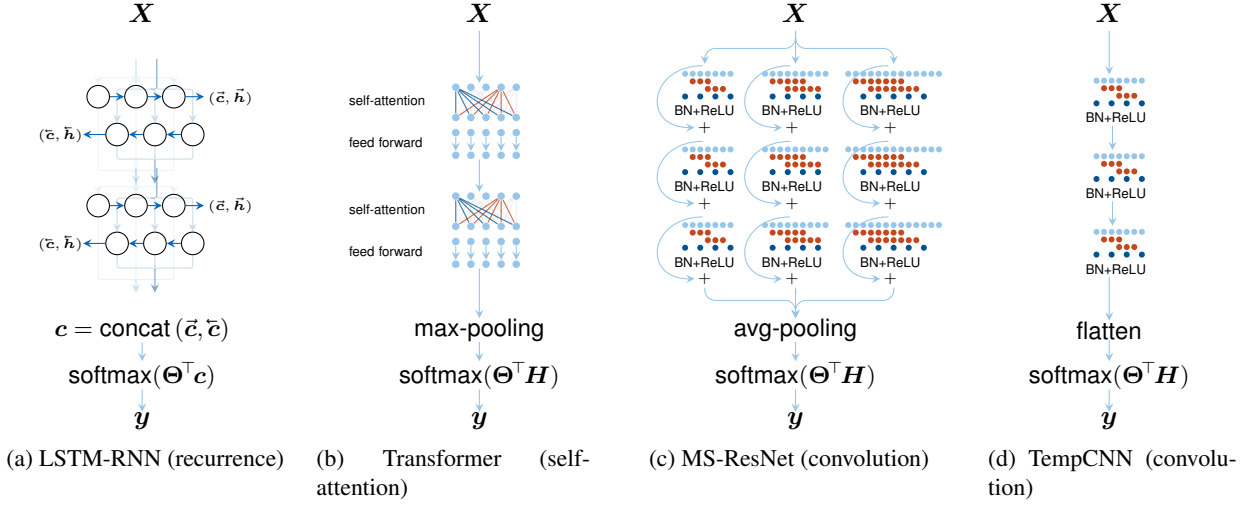


Figure 2: A schematic overview over the four network topologies used in this study.

with zero-valued vectors. The last hidden states from forward and backward passes, \vec{c} and \bar{c} , are concatenated and produce final classification scores via a dense output layer with softmax activation function. This network architecture is illustrated in Fig. 2a We tuned the conditionality of hidden states $D_h \in \{2^4, 2^5, \dots, 2^8\}$, the number of recurrent layers $L \in \{1, 2, \dots, 7\}$, and applied dropout $p_{\text{drop}} \in [0, 1]$ between the recurrent layers at training time.

4.2. Transformer

For the self-attention model, we adopted the encoder architecture of the self-attention Transformer network [44], as illustrated in Fig. 2b. We discarded the step of word embedding, as the satellite time series data lives in a continuous space of spectral reflectance values. Following Vaswani *et al.* [44], we added a positional encoding to the time series, since self-attention can not utilize the sequential correlation of time series. Subsequently, the time series with positional encoding is transformed into higher-level D -dimensional feature representations through L transformer blocks. Each block encodes features through a multi-head self-attention mechanism followed by multiple dense layers applied to each time instance independently. Skip connections are introduced between the layers and layer normalization is used throughout the model. We refer to [44] for a detailed description of the layer topology. The representation of the last layer $\mathbf{H} \in \mathbb{R}^{H \times T}$ is then reduced to $\mathbf{h} \in \mathbb{R}^D$ by a global maximum pooling through the time dimension. This reduced representation is then projected to scores for each class by a final fully-connected layer with a softmax activation function.

For this architecture, we tuned the dimensionality of the hidden states $D_h \in \{2^4, 2^5, \dots, 2^8\}$, the number of self-attention layers $L \in \{1, 2, \dots, 8\}$, and the number self attention heads $H \in \{1, 2, \dots, 8\}$ that determine the number of self-attention mechanisms applied in parallel.

4.3. Multi-Scale Residual Networks

Residual Networks (ResNets) [41] are a common backbone architecture in computer vision. They consist of residual blocks $f_{\Theta}^{\text{cbn}} = f_{\Theta}^{\text{c}} \circ f^{\text{b}} \circ f^{\text{r}}$ of convolution layers f_{Θ}^{c} and batch normalization layers f^{b} [77], followed by a *Rectified Linear Unit (ReLU)* activation function f^{r} . Characteristically, in each block $\mathbf{H} = f_{\Theta}^{\text{cbn}}(\mathbf{X}) + \mathbf{X}$, the encoded feature representation $f_{\Theta}^{\text{cbn}}(\mathbf{X})$ is added to the identity mapping of the input. This forms residual skip connections where each residual layer numerically adds higher-level features to the forward propagated representation. These skip connections aid gradient backpropagation through the network and allow the training of very deep models.

These convolutional residual connections have been adapted to time series classification [78] where 2D convolutions through the spatial dimensions are replaced by 1D convolutions through time. Since convolutional layers, by design, extract features from the local (temporal) neighborhood, architectures that process time series at multiple

scales [79] have shown good results on time series benchmark datasets [80; 81]. In this work, we utilize the architecture proposed by Wang *et al.* [78]⁴ where an input time series $\mathbf{X} \in \mathbb{R}^{(T=512) \times D_{\text{in}}}$ is processed in three separate streams of each three residual blocks with increasing convolutional kernel sizes $K^c \in \{3, 5, 7\}$. Hence, each stream extracts features at a different temporal scale, as drawn in Fig. 2c. The representation after each stream is then average-pooled with pooling kernel sizes $K^p \in \{16, 11, 6\}$, yielding three feature representations $\mathbf{h}^{K^c=3}, \mathbf{h}^{K^c=5}, \mathbf{h}^{K^c=7} \in \mathbb{R}^{D=256}$, and concatenated to a common representation $\mathbf{H} \in \mathbb{R}^{D=768}$. A final fully connected layer with softmax activation function reduces this vector to individual activation scores per class. Note that the design of this network requires a fixed sequence length of $T = 512$. To obtain this sequence length, we interpolated the satellite time series by the nearest neighbor method. Since the architecture is precisely-defined in the original implementation, we solely tune the number of convolutional kernels $D_h \in \{2^4, 2^5, \dots, 2^8\}$ for this architecture.

4.4. TempCNN

Recently, the temporal convolutional neural network (TempCNN) [69] has been proposed and evaluated specifically for the purpose of crop type mapping. It is a comparatively light-weight architecture of three sequential 1D convolutional layers followed by batch normalization, a ReLU activation function, and dropout. The encoded features are flattened and passed to a final fully connected layer with batch normalization, ReLU activation function, and dropout, as shown in Fig. 2d. These features are then projected to scores per class using a final fully connected layer and softmax.

The tuneable hyperparameters of this model are the number of convolutional kernels $D_h \in \{2^4, 2^5, \dots, 2^8\}$ that determine the dimensionality of hidden states, the respective kernel sizes $K \in \{3, 5, 7\}$, and the dropout probability $p_{\text{drop}} \in [0, 1]$.

4.5. DuPLO

The *DUAL view Point deep Learning architecture for time series classificatiOn* (DuPLO) [59] model is a complex deep learning model designed for crop type classification from sequences of small satellite images of five by five pixels. Since we do not use sequences of images in this work, we treated the time series as a single-pixel images. It consists of two streams. A three-layer CNN stream uses 2d convolutions to aggregated spatial features independently of time. The second stream implements a 2D-CNN encoder and mono-directional RNN layer implemented by a Gated Linear Unit (GRU) [62] for temporal characteristics. The recurrent neural network features $\mathbf{H} \in \mathbb{R}^{H \times T} \mapsto \mathbf{y} \in \mathbb{R}^H$ are then aggregated via a simplified soft-attention mechanism [76], described in Section 3.5. According to the authors, this model requires a special training procedure through additional weighted auxiliary losses from additional dense layers for each stream to simplify gradient propagation through.

4.6. Random Forests

As shallow learning baseline, we tested a *Random Forest (RF)* model using the `scikit-learn` framework [82]. We augmented the raw reflectance input features by additional spectral indices, since feature extraction is usually required for a good performance. Hence, we added the features *Normalized Difference Vegetation Index (NDVI)*, *Normalized Difference Water Index (NDWI)*, *Brightness Index (BI)*, *Inverted Red-Edge Chlorophyll Index (IRECI)*, and *Enhanced Vegetation Index (EVI)* to the time series data. Overall, the random forest model receives a flattened vector of all spectral values for each time. This results in a raw feature vector $\mathbf{x}_{\text{raw}} \in \mathbb{R}^{1260}$ (70 times each 13 spectral bands and 5 spectral indices) and $\mathbf{x}_{\text{pre}} \in \mathbb{R}^{345}$ (23 times each 10 spectral bands and 5 indices). Also note, that we did not obtain satisfactory results on the random forest using the entire body of the dataset likely due to class imbalance of the labels. Hence, we chose to sample a more uniform subset of up to 500 time series per class to train and test the random forest model. We argue that this would rather advantage random forest in the classification results (especially for the macro accuracies).

We tuned the number of trees $\{200, 400, \dots, 2000\}$, the number of features to be considered at every split $\{\text{auto}, \text{sqrt}\}$, the maximum depth the the trees $\{10, 20, \dots, 110\}$, the minimum number of samples required to split a node $\{2, 3, \dots, 10\}$, the minimum number of samples required at each leaf node $\{1, 2, 3, 4\}$, and whether or not to use bootstrapping $\{\text{true}, \text{false}\}$.

⁴Original implementation available at <https://github.com/geekfeiw/Multi-Scale-1D-ResNet>

5. Training Details

We trained the LSTM-RNN, MS-ResNet, and TempCNN models via mini-batch stochastic gradient descent with gradients scaled using the Adam optimizer [83] with momentum parameters $\beta_1 = 0.9$, and $\beta_2 = 0.98$. The learning rate and weight decay parameters were sampled from log-uniform distributions over $[10^{-8}, 10^{-1}]$ and $[10^{-12}, 10^{-1}]$, respectively, and determined via hyperparameter tuning, as described in Section 6. Following Vaswani *et al.* [44], we employed a learning rate scheduler for the Transformer model where the learning rate is first increased linearly for $N_{\text{warmup}} \in \{10^1, 10^2, 10^3\}$ gradient steps and then decayed exponentially. We stopped training early when the loss did not decrease over an average of the last 10 epochs. This condition must have been true for five epochs in a row to stop the training process.

6. Model Selection

The model architectures and training procedures depend on a variety of hyperparameters that may vary based on the objective and the dataset. We described the tuneable hyperparameters for each model in the previous sections. These were, for the deep learning models, the dimensionality of the hidden vectors, the number of layers, the number of self-attention heads, the convolutional kernel sizes, the dropout probability, the number of transformer warmup steps, the learning rate, and the weight decay rate. To determine the optimal set of parameters, we sampled candidate hyperparameters from a hyperparameter space, trained on a subset of the training partition, and evaluated the performance on a validation set. The partitioning scheme and spatial separation of the datasets are described in Section 7. Here, we first sampled hyperparameters from the search space at random for the first 34 models and recorded the validation performance measured in terms of the kappa metric [84]. Based on these initial points, a kernel density estimate scaled by the validation performance of the model determined a probability distribution that was used to sample the next best set of hyperparameters, following the protocol suggested by Bergstra *et al.* [85] and implemented using their HYPEROPT framework. We combined this with an *asynchronous successive halving* strategy [86]. This algorithm splits the 60 training epochs into four brackets with a grace period of 10 epochs. After each bracket, only the best-performing half of the models continued training, while the other runs were stopped at the end of each bracket. Both of these were implemented using the RAY-TUNE framework [87] that allows hyperparameter training of four models in parallel per GPU on a NVIDIA-DGX1. For each model architecture, we evaluated on 300 sets of hyperparameters for both preprocessed and raw datasets having resulted in 2400 model evaluations.

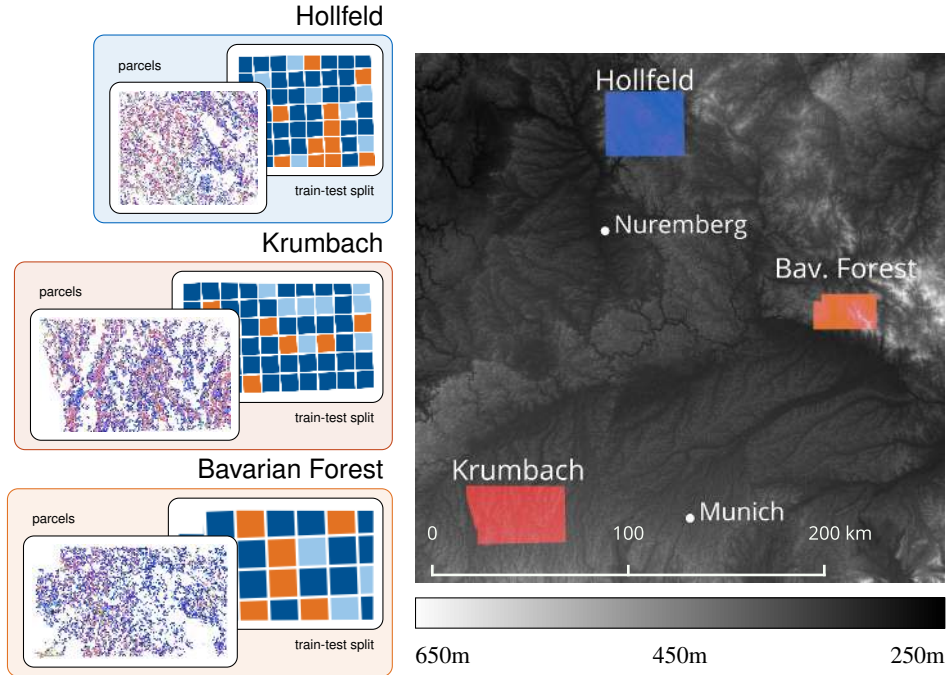
The hyperparameters of the RF models were determined through a random search on 300 runs with three-fold cross-validation. To reduce tuning time and the class imbalance in the data, we used only up to 500 samples per class. The architecture of the DuPLO model was precisely-defined in [59] with detailed specifications for hidden dimensions, learning procedure and learning rate. Hence, we employed the model directly as specified.

7. Data

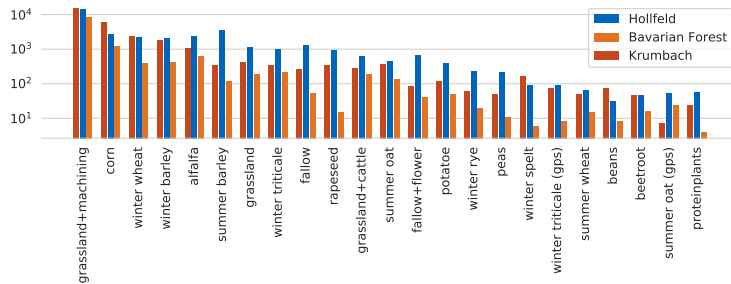
We evaluated the mechanisms described in Section 3 that were implemented in the models of Section 4 on the task of crop type identification. Crop type identification is a sub task of land cover and land use classification where the model has to extract classification-relevant features and learn a discriminative decision function to separate the classes of vegetation. We analyze the extracted features later in Section 8.6. Vegetation life cycle events, known as phenology, provides a distinctive temporal signal to identify types of vegetation using a limited set of spectral channels. This makes the temporal signal a key source of relevant features when learning a discriminative model to differentiate various types of vegetation and thus well-suited to test the mechanisms and models of this work.

We focus on three spatially separate regions in Bavaria, as shown in Fig. 3. These regions are *Hollfeld* in Upper Franconia, *Krumbach* in Swabia, and a northeastern portion of the *Bavarian Forest*. These regions are located in approximately 100 km distance from each other. While the climate conditions are comparatively similar, different elevations and soil conditions favor differences in the distribution of cultivated crops, as can be observed from the class distribution histograms in Figs. 3b and 3c.

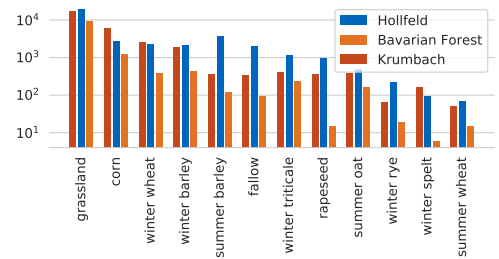
The label data for this study originates from a joint cooperation project with the *Bavarian State Ministry of Food, Agriculture and Forestry (StMELF)* and the German remote sensing company *GAF AG*. This enabled us to obtain two Sentinel 2 time series datasets from the same field parcels. These are one dataset with raw top-of-atmosphere



(a) The three areas of interest in Bavaria, Hollfeld, Krumbach and Bavarian Forest are located in different regional environments indicated by the elevation map. We show the field parcels colored by crop type, along with the random train test split for each of the regions.



(b) Class frequencies per region on a 23 class partition



(c) Class frequencies per region on a 12 class partition

Figure 3: Test regions for labels and satellite time series

Sentinel 2 observations acquired with minimal effort from Google Earth Engine, as described in Section 7.2.1, and one preprocessed time series dataset provided by GAF AG which can be considered prototypical for the industry-standard, as outlined in Section 7.2.2.

To obtain spatially separate partitions [88] for *training* of model parameters using gradient descent, *validation* of hyperparameter sets and final *evaluation* of the model, we divided the three regions further into rectangular blocks of $4500 \text{ m} \times 4500 \text{ m}$ with a 500 m margin between blocks, as shown in the train-test split in Fig. 3a. These blocks were randomly assigned to training, validation, and evaluation partitions obeying a 4:1:1 ratio which resulted in 94, 21, and 29 blocks respectively. We decided for such a block-wise spatial separation in order to enforce independence of the dataset partitions without implicit overfitting, as experimentally evaluated and observed in previous work [54] and as recommended for geospatial data by further studies [89; 88] focusing the implicit bias of spatial auto-correlation.

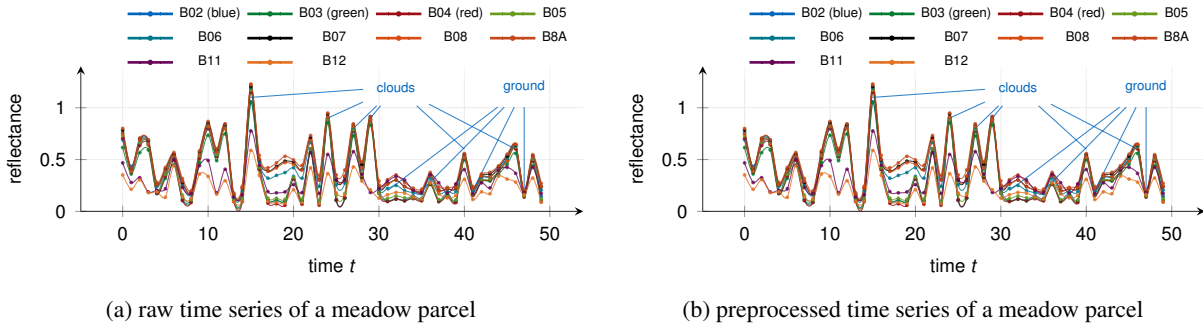


Figure 4: An illustration and comparison of a raw and a preprocessed Sentinel 2 time series of the same meadow field parcel. Preprocessing allows for a visual interpretation. The onset of growth after timestep $t = 5$ is clearly visible. Also, several cutting events can be observed over the time of the vegetation period. The preprocessed time series, however, contains repeated values due to temporal interpolation and cloud removal. In the raw time series, most information from the measured signal is retained. Noise caused by, *e.g.*, atmospheric effects and clouds, obscures the phenological events.

7.1. Crop Type Labels

The *Common Agricultural Policy* of the European Union subsidizes farmers based on the type of crops they cultivated. Each member country is required to gather geographical information of the geometry of the parcel and the type of crop. This information is provided by obligatory surveys, as part of the subsidy application process, directly from the farmers. National agencies monitor the correctness either by gathering control samples *in-situ* or by utilizing remote sensing and Earth observation technology.

The crop label categories provided for this study were provided by StMELF. They follow a *long-tailed class distribution* with more than 269 distinct categories. Here, the most common 15, 26, and 62 categories cover 90%, 95%, and 99% of the field parcels, respectively. In cooperation with StMELF and GAF, a set of land-use and land-cover categories was aggregated and selected with respect to the aims and objectives of the ministry. From this aggregation, we selected two labeled datasets: The first one contains 23 classes, as shown in Fig. 3b, and resembles the land-use of the parcels. These categories cover, for instance, multiple types of grassland. This dataset is a challenging to classify, since multiple categories (*e.g.*, grassland for cattle-use and for machining) share similar surface reflectance features measured by the satellite. We also aggregated these categories further into a second dataset that focuses on 12 land cover categories, as shown in Fig. 3c. By evaluating models on two 23-class land-use categorization and 12-class land cover categorization datasets, we aimed at reporting model accuracies from two objectives of different difficulty.

7.2. Satellite Data

We utilized data from the optical Sentinel 2 satellite constellation that consists of two satellites orbiting the Earth in a sun-synchronous orbit on opposite tracks. These satellites observe the same spot on the Earth’s surface every 2 to 5 days, depending on the latitude. The data is acquired by a line-scanner capturing 13 spectral bands, ranging from ultra-violet wavelengths, for observing atmospheric water vapor, over optical and near-infrared wavelengths, sensitive to chlorophyll and photosynthesis, up to short-wave infrared wavelengths, that are sensitive to soil moisture. In regions where the sensor strips overlap, we observed approximately 140 measurements of the same point during the entire year of 2018, while on the stripe centers we only recorded 70 observations within the same time range.

7.2.1. Raw Dataset

For the raw Sentinel 2 dataset, we utilized the *top-of-atmosphere* reflectance values at the processing level L1C. This data was acquired from *Google Earth Engine* [90] and queried for each field parcel individually. Pixels located within the boundaries of a field parcel were mean-aggregated into a single feature vector of 13 spectral bands at each time. We show examples of a meadow parcel of the raw Sentinel 2 time series in Fig. 4a. Note that cloud coverage, visible as positive peaks within the reflectance profiles, dominates the signal and makes a visual interpretation of this

Table 1: Comparison of models on preprocessed (pre) and raw dataset on the 23-class land use and the 12-class land cover categorization. The values reported are the mean and standard deviation of three models with the best, second and third-best hyperparameter sets trained on the training and validation partitions and tested on the evaluation partition.

| (a) Kappa metric 23-class dataset | | | | | | |
|-----------------------------------|------|-----------------------------------|-----------------------------------|-------------|-----------------|-----------------|
| κ | RF | LSTM-RNN | Transformer | DuPLO | MS-ResNet | TempCNN |
| pre | 0.76 | 0.78 ± 0.01 | 0.79 ± 0.03 | 0.81 | 0.76 ± 0.03 | 0.80 ± 0.00 |
| raw | 0.53 | 0.71 ± 0.01 | 0.71 ± 0.03 | 0.68 | 0.69 ± 0.03 | 0.67 ± 0.02 |

| (b) Kappa metric 12-class dataset | | | | | | |
|-----------------------------------|------|-----------------------------------|-----------------|-------------|-----------------|-----------------|
| κ | RF | LSTM-RNN | Transformer | DuPLO | MS-ResNet | TempCNN |
| pre | 0.86 | 0.87 ± 0.01 | 0.87 ± 0.04 | 0.89 | 0.85 ± 0.01 | 0.88 ± 0.03 |
| raw | 0.62 | 0.83 ± 0.01 | 0.82 ± 0.02 | 0.78 | 0.78 ± 0.02 | 0.71 ± 0.07 |

| (c) Overall accuracy metric 23-class dataset | | | | | | |
|--|------|-----------------------------------|-----------------|-------------|-----------------|-----------------------------------|
| acc. | RF | LSTM-RNN | Transformer | DuPLO | MS-ResNet | TempCNN |
| pre | 0.83 | 0.85 ± 0.01 | 0.85 ± 0.02 | 0.86 | 0.83 ± 0.02 | 0.86 ± 0.00 |
| raw | 0.71 | 0.81 ± 0.01 | 0.80 ± 0.02 | 0.79 | 0.79 ± 0.03 | 0.79 ± 0.00 |

| (d) Overall accuracy metric 12-class dataset | | | | | | |
|--|------|-----------------------------------|-----------------------------------|-------------|-----------------|-----------------------------------|
| acc. | RF | LSTM-RNN | Transformer | DuPLO | MS-ResNet | TempCNN |
| pre | 0.91 | 0.92 ± 0.01 | 0.92 ± 0.03 | 0.92 | 0.91 ± 0.01 | 0.92 ± 0.02 |
| raw | 0.80 | 0.90 ± 0.00 | 0.89 ± 0.01 | 0.87 | 0.87 ± 0.01 | 0.83 ± 0.04 |

| (e) Class-mean f_1 score 23-class dataset | | | | | | |
|---|------|-----------------|-----------------------------------|-------------|-----------------|-----------------|
| f_1 | RF | LSTM-RNN | Transformer | DuPLO | MS-ResNet | TempCNN |
| pre | 0.38 | 0.47 ± 0.02 | 0.50 ± 0.06 | 0.55 | 0.49 ± 0.03 | 0.50 ± 0.02 |
| raw | 0.18 | 0.43 ± 0.01 | 0.45 ± 0.06 | 0.34 | 0.44 ± 0.01 | 0.36 ± 0.01 |

| (f) Class-mean f_1 score 12-class dataset | | | | | | |
|---|------|-----------------|-----------------------------------|-------------|-----------------|-----------------|
| f_1 | RF | LSTM-RNN | Transformer | DuPLO | MS-ResNet | TempCNN |
| pre | 0.55 | 0.60 ± 0.02 | 0.66 ± 0.07 | 0.66 | 0.64 ± 0.02 | 0.60 ± 0.06 |
| raw | 0.34 | 0.63 ± 0.01 | 0.64 ± 0.07 | 0.51 | 0.55 ± 0.04 | 0.41 ± 0.07 |

time series difficult. This time series dataset is challenging to classify but can be acquired at minimal effort. Hence, we benchmarked our models on this harder objective.

7.2.2. Preprocessed Dataset

For further evaluation, we had access to a second dataset that originates from the same publicly available top-of-atmosphere data products. In contrast to the raw data set, this data was processed by GAF through their tested and operational preprocessing engine. This process includes common preprocessing techniques, such as, *e.g.*, atmospheric correction, temporal selection of cloud-free observations, a focus on observations of the vegetative period, and cloud masking. We show an example of the preprocessed dataset in Fig. 4b compared to the identical parcel in Fig. 4a. Here, the cloudy observations have been identified and filtered by a separate cloud classification model. This makes this dataset easier to classify by shallow models, as distinctive phenological features, *i.e.*, onset of growth and cutting of the meadows, can be visually distinguished. Overall, this preprocessing pipeline can be considered prototypical for an industry standard but requires significant computational and design effort to generate.

8. Experiments and Results

In this section, we experimentally compare the transformer model, that is based on self-attention, to a recurrent neural network and two convolutional neural networks, as described in Section 4. This experimental section is structured in three parts: First in Section 8.1, we show quantitative results on all evaluated neural network architectures. Here, we present results on preprocessed and raw Sentinel 2 data described in Section 7.2 and on two sets of categories. One 23-class categorization evaluates model performance on land use classification while the other 12-class categorization focuses on land cover. Next in Section 8.3, we analyze the ability of the models to suppress noise, *e.g.*, induced by clouds, in raw time series data by a feature importance analysis based on gradient backpropagation. Finally in Sections 8.4 and 8.6, we focus specifically on the self-attention mechanism and analyze activation scores and internal states of the transformer model in detail.

8.1. Quantitative Model Evaluation

We compared the performance of the deep learning models LSTM-RNN [61], Transformer [44], MS-ResNet [78], the DuPLO model [59], and TempCNN [69], as well as a Random Forest (RF) classifier as shallow baseline. We

determined the optimal hyper-parameters separately for preprocessed and raw Sentinel 2 time series datasets, and for the 23 and 12 class categorizations, as described in Section 6. For each experiment, we trained and evaluated three different models with the best, second-best, and third-best hyperparameter configuration and random seeds for parameter initialization and composition of the training batches. In Table 1, we present the mean and standard deviation of the accuracy metrics from these three results. All models were trained and evaluated on block partitions for training and evaluation (*cf.* Fig. 3) in all three regions Hollfeld, Krumbach and Bavarian forest. We evaluated these models on raw and preprocessed satellite time series on identical field parcels.

It is noteworthy that the overall accuracy measure, as presented in Tables 1c and 1d, over-represents frequent classes. Since the datasets used for this study show a heavily imbalanced class distribution, the accuracy of frequent classes dominates this metric. Nevertheless, it is an intuitive measure and a good representation of the example-wise accuracy, representative of the visual impression from observing a spatial map classification. To account for the less frequent classes, we also report Cohen’s kappa metric [84] in Tables 1a and 1b. This is a correlation score that is frequently used in remote sensing and normalizes the classification scores by the probability of a random chance prediction based on empirical class frequencies. As a further measure of performance, we report the f_1 score, *i.e.*, the harmonic mean of precision and recall, for each class and average over all classes in Tables 1e and 1f. By doing so, all classes get equally weighted disregarding the the number of samples per category. The class-mean f_1 scores are generally lower than accuracy and kappa, as we chose a large set of classes where some classes semantically overlap or only have few examples which make it difficult for a data-driven neural network to learn feature extraction and decision function. Overall, we aimed at comparing different properties of the classification models. Hence, the overall accuracy reflects the classification accuracy per field parcel, while the f_1 score measures the accurate classification of all classes.

Table 1 reveals that data preprocessing had a positive effect on the accuracy, f_1 score, and kappa of all models. It seems that the manual supervision during preprocessing improved the classification performance. This better performance on pre-processed time series is, to a certain degree, expected, since this preprocessing makes a visual identification of classification relevant events possible, as could be seen in Fig. 4b. Comparing the visual examples at Fig. 4 suggests that the classification of the preprocessed datasets is an easier task than approximating preprocessing-like mechanism jointly together with classification in a holistic end-to-end model. Overall, the region- and domain-specific expertise needed to design such preprocessing pipelines increases the classification performance compared to classification of the raw datasets were the deep learning models have to learn preprocessing-like mechanisms solely based on the provided examples without access to model knowledge. This holds especially true if the number of samples is limited, some examples are falsely labeled, or the semantic representation of classes do overlap. Considering this, it is notable that the LSTM-RNN and Transformer models performed competitively well on raw data compared to pre-processed data. Especially in the 12-class land cover categorization setting, the difference in performance was rather minor, speaking of 5 % in accuracy and 0.03 in kappa score. In terms of the f_1 score, the LSTM-RNN variant even achieved better performance on raw data compared to preprocessed data, while is ranging behind the Transformer . Throughout both the 23-class dataset (*cf.* Tables 1a, 1c and 1e) and 12-class dataset (*cf.* Tables 1b, 1d and 1f) variants, all evaluated deep learning models performed similarly well on preprocessed data. Interestingly, for the raw dataset partitions, the LSTM-RNN and Transformer models achieved slightly better accuracy, kappa, and f_1 scores values compared to the MS-ResNet and TempCNN variants. In the 23-class setting, the difference is rather small with 1–2 % in overall accuracy and 0.01 in kappa score which seems not significant considering their reported variances. The 12-class case, however, confirms this observation with a more pronounced difference of 0.03–0.07 in kappa metric and 5 % and 11 % in accuracy. In the next Section 8.3, we will investigate this further by a feature importance analysis monitoring the backpropagation process.

When comparing the f_1 scores in Tables 1e and 1f with the accuracy scores in Tables 1c and 1d on raw data, we see that the convolutional TempCNN model showed similar performance compared to the MS-ResNet model. The f_1 scores, however, show a lower score for TempCNN . From these metrics, we can derive that the TempCNN did classify the majority of field parcels accurately but achieved lower accuracies on some of the more infrequent class categories compared to MS-ResNet . This may be attributed to the shallower network topology. The DuPLO achieves very good classification accuracy on preprocessed satellite data, as it is on par with the other models. Since the model architecture is precisely defined by the authors, we could not run the model with different hyper parameter settings. Still it outperforms the other models in some tasks on preprocessed data, see Tables 1a, 1b and 1e. On the raw satellite data, it is behind Transformer and LSTM-RNN models.

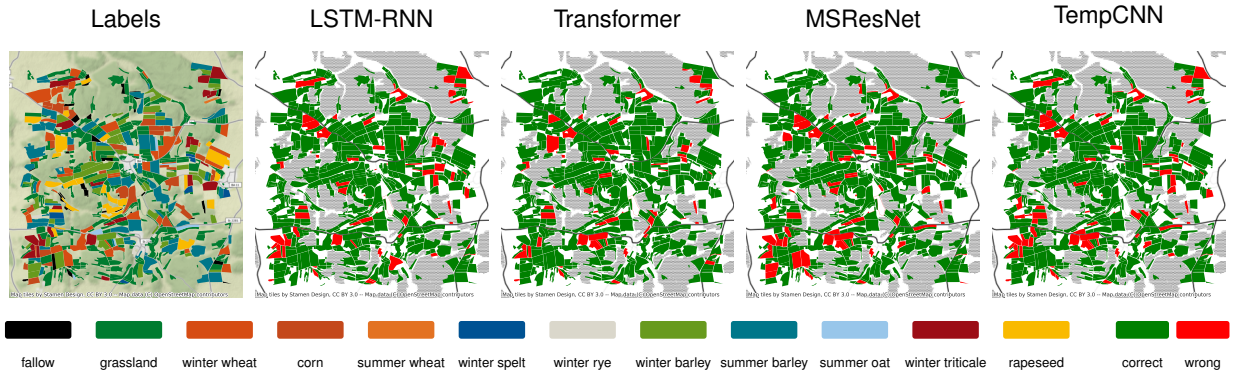


Figure 5: Qualitative comparison of the classification models from region in 4430000 E/W, 5528000 N/S in EPSG:31468

Interestingly, the random forest baseline achieved competitive results to the deep learning models on preprocessed time series data. It appears that preprocessing, as a form of feature extraction, helped the random forest classifier to improve its performance significantly. Without data preprocessing on the raw dataset, the random forest baseline fell behind the deep learning models. The kappa metric—that ranged 0.15 worse in the 23-class land use variant and 0.1 to 0.2 worse in the 12-class land use variant—indicates that infrequent classes were classified less accurately by the random forest classifier. This got further confirmed by the poor f_1 score throughout both dataset variants where the random forest achieved worse performance on raw datasets compared to preprocessed datasets. Overall, this stresses the necessity of feature extraction for shallow machine learning methods while demonstrating that—with sufficient manual effort in preprocessing and, thus, feature extraction—random forests can achieve competitive accuracies.

It may be concluded that the region- and domain-specific expert knowledge in data preprocessing helped all models to achieve better accuracies compared to the raw sentinel 2 time series dataset. All models achieved similar accuracies for preprocessed datasets. Even the random forest classifier showed a competitive performance to the deep learning models with similar scores in overall accuracy, slightly worse kappa and f_1 scores. Both, the LSTM-RNN and Transformer models, that rely on recurrence and self-attention, achieved better accuracies on raw time series data compared to the convolutional models MS-ResNet and TempCNN. This effect was minor in the land-use categorization with 23-classes and more pronounced in the land-cover categorization, but overall consistent throughout this evaluation. We will investigate the difference of recurrence and self-attention compared to convolution further in the next section.

8.2. Qualitative Model Evaluation

We conduct a qualitative analysis in addition to the quantitative model comparison in model analysis in Section 8.1 and Table 1. Here, we use the deep learning models to predict the 12 land cover classes on the raw time series dataset. Each time series, as in Fig. 4a, was obtained from the reflectance values aggregated over one field geometry, as shown in the left-most figure. The parcels were colored by crop type and were obtained from 4500m by 4500m block (4430000 E/W, 5528000 N/S in EPSG:31468) from the test partition. The figures towards the right show the fields that were correctly and wrongly classified by the respective models. As indicated by Table 1, the classification accuracies do not vary significantly throughout the models so that no clear advantage between models is visible.

8.3. Temporal Feature Importance Assessment by Gradient Backpropagation

In the previous section, we observed that models based on recurrence and self-attention achieved better accuracy metrics on noisy raw data compared to convolutional models. Here, we investigate this further through a simple, yet effective, feature importance analysis based on gradient backpropagation.

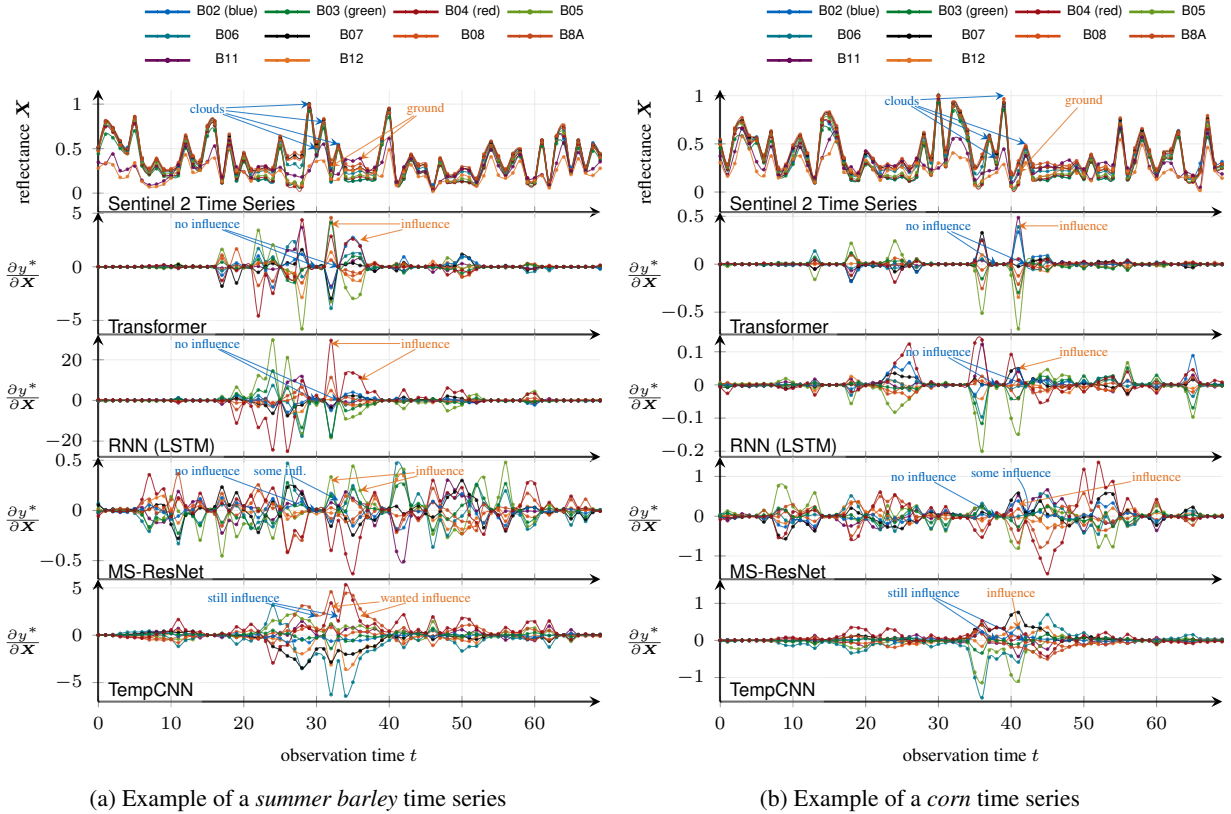


Figure 6: Input feature importance analysis by gradients of the input time series \mathbf{X}

Deep learning models are differentiable functions f_{Θ} that approximate a mapping from an input tensor \mathbf{X} to a ground truth tensor \mathbf{y} , as detailed in Section 3. In the training process, gradients are backpropagated using Eq. (1) in order to adjust the model weights Θ . Since the model f_{Θ} is fully differentiable, we can use the same mechanism to back-propagate gradients further up to the input tensor \mathbf{X} . When we start from the highest predicted score $y^* = \max(\hat{\mathbf{y}})$, we can propagate gradients through the entire network back to the individual elements $\mathbf{x}_t = (x_t^{B01}, x_t^{B02}, x_t^{B03}, \dots)^T$ of the input tensor $\mathbf{X} = (\mathbf{x}_0, \dots, \mathbf{x}_T)$. These gradients $\frac{\partial y^*}{\partial \mathbf{X}}$ reflect the influence of each input data element on the current class prediction. Vanishing gradients indicate that any change in the input has no effect on the prediction. Positive or negative gradients would suggest an increase or decrease of the predicted score if the input changed at these times. We would like to emphasize that this analysis is model-agnostic, can be implemented in few lines of code in current deep learning frameworks that utilize automatic differentiation, and does not require ground truth labels.⁵

For this experiment, we estimated the influence of each input time step on the classification prediction for each of the evaluated networks, *i.e.*, LSTM-RNN (recurrence) and Transformer (self-attention), as well as MS-ResNet and TempCNN (convolution). Figure 6 illustrates this by means of two separate examples of two corn- and summer barley parcels. The top figures each show the input time series \mathbf{X} as a sequence of raw Sentinel 2 reflectances over the year of 2018. In the raw time series, we can identify atmospheric noise and clouds as positive peaks in the data. These are caused by the high reflectance values of clouds throughout all spectral bands. The presence of a cloud at a given point in time does not provide any additional information about the covered surface and should be, thus, considered irrelevant for the classification. The following rows display the gradients $\frac{\partial y^*}{\partial \mathbf{X}}$ for each of the respective models. These plots indicate the influence of the measurement at the particular input time in the top row on the classification prediction of the respective model.

⁵Our implementation is available at <https://github.com/marccoru/crop-type-mapping/blob/master/notebooks/FeatureImportance.ipynb>

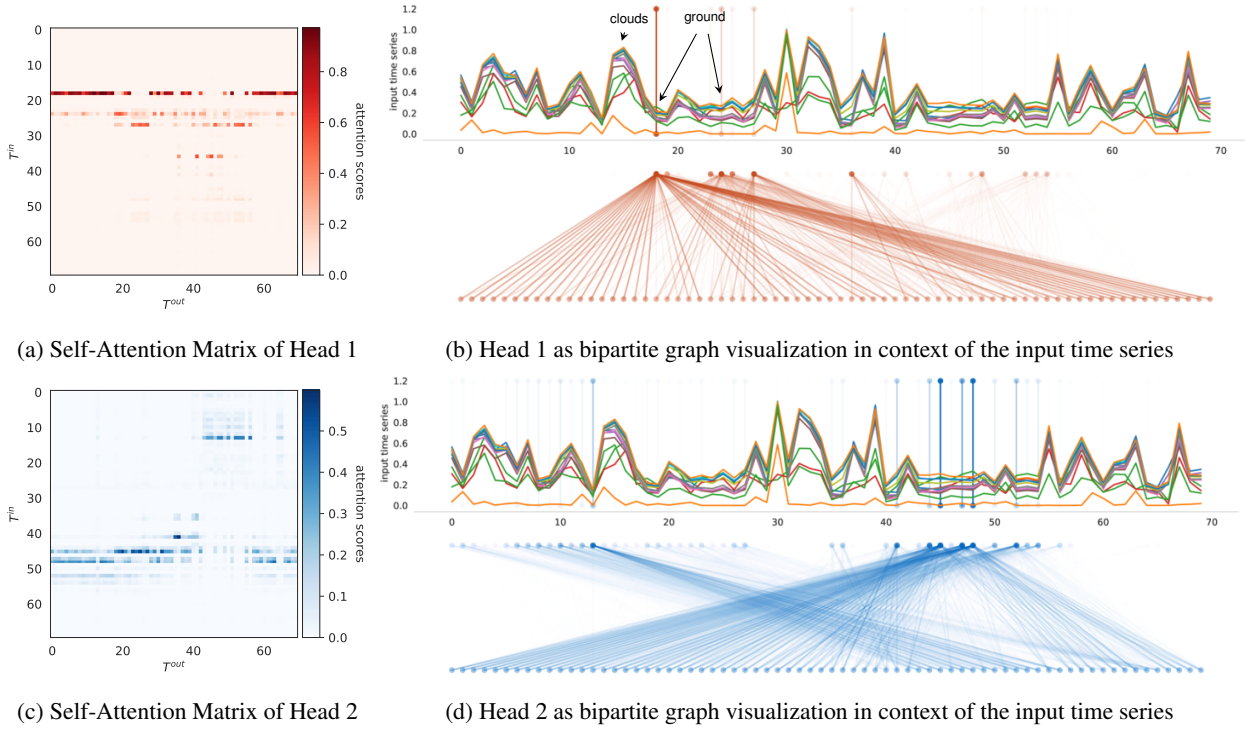


Figure 7: Visual illustration of the self-attention scores from a pre-trained transformer self-attention model

The results of this experiment shows that the gradients through the LSTM-RNN and Transformer networks were only non-zero for comparatively few observations. This indicates that only a few key time-points were necessary to extract the classification relevant information from the raw time series. Only time points where the surface was not obscured by clouds had non-zero gradients. Time instances with positive peaks in reflectance, likely induced by clouds, did not have influence the classification prediction, as indicated by vanishing gradients. This experimentally shows that the LSTM-RNN and Transformer models have been optimized to automatically identify and suppress time instances that are not classification relevant, *e.g.*, though cloud coverage, learned purely from data.

The convolution-based model architectures MS-ResNet and TempCNN show, in general, a similar behavior. However, these models seem to have some non-zero gradients on cloudy observations. This is especially true for the comparatively shallow TempCNN architecture where the cloudy observations at $t = 30$ in Fig. 6a and $t = 38$ in Fig. 6b still have influence in the classification prediction. The MS-ResNet model also seems to be able to extract features from the entire temporal range. Since the data ranges from January to December, it is expected that the particular crop class is only visible during the summer periods. The MS-ResNet model seems to still include features from the winter periods.

Summarizing the above, the recurrence and self-attention based models LSTM-RNN and Transformer seem to extract selective temporal features, while the convolution-based models utilize the entire time series. Also, the LSTM-RNN and Transformer models were able to transition from a time observation with high gradients to zero gradients without any time delay. It appears that the convolution-based models TempCNN and MS-ResNet require at least two subsequent observations to reduce the influence of the particular time instance. This can be observed from Fig. 6a at $t = 30$ and $t = 34$: The MS-ResNet model could reduce the influence of the observations at $t = 30$ (indicated by zero gradients) when three subsequent observations were cloudy. However, when only one observation was cloudy, as in $t = 34$, MS-ResNet was unable to suppress this observation completely. In contrast, the models LSTM-RNN and Transformer were able to suppress these cloudy observations even if they appeared in a single time instance.

We attribute this difference in the influence of input observations to the respective mechanisms for feature extraction. Recurrent networks utilize internal gates that can control the influence of the particular time instance to a hidden

memory state. Our previous work [66], which visualized internal LSTM states, supports this hypothesis for recurrence. Similarly, self-attention enables a model to select specific observations by assigning a large attention score to them. In contrast, convolutions always extract features from a local neighborhood. Hence, it seems to be more difficult for convolutional architectures to ignore sudden appearances of irrelevant observations within a temporal sequence, as indicated by the non-zero gradients at cloudy observations.

8.4. Qualitative Analysis of Self-Attention Scores

In the previous section, we experimentally observed that the Transformer model was able to suppress the influence of an observation for classification-irrelevant observations, *e.g.*, clouds. Here, we concentrate on the self-attention mechanism (*cf.* Section 3.4) that was implemented in the Transformer model and analyse the attention scores on the example of the cornfield parcels from the previous experiment in shown in Fig. 6b.

The Transformer models realize multi-headed self-attention as multiple attention mechanisms in parallel. To recall, every self-attention mechanism calculates an attention matrix $\mathbf{A} \in [0, 1]^{T \times T}$ using the softmax operation following Eq. (3). These attention scores define the influence of an input time feature on a higher-level output time feature. We visualize the values of this matrix in Figs. 7a and 7c for three attention heads from the first self-attention layer (of three). This matrix can be seen as an adjacency matrix between input nodes and output nodes. In Figs. 7b and 7d, we alternatively show the same matrix as bipartite graphs. The former matrix elements are now shown as weighted directed edges between input and output nodes. The strength of the attention is indicated by the opacity of the edge. Above the attention graph, we show the input time series of the example as a reference to allow for visual interpretation of the time instances. Here, the attention scores are drawn as vertical lines corresponding to the values in \mathbf{A} .

From these figures, we can directly observe that the self-attention scores focus on distinct events with each head. While the first head appears to focus on the early-middle part of the time series, the second head extracts features from the early and late time series. Also, the attention scores seem to re-distribute features over time. Hence, even though hidden feature tensors throughout the network still maintain a temporal dimension, the temporal consistency with the input time series loses context. Consistent with the previous experiment in Section 8.3, we observed that the attention scores did not focus on the strong positive peaks in the time series which indicate a cloudy observation. Hence, we can conclude that self-attention mechanisms are a key tool in suppressing the non-classification-relevant cloudy observations which explain the zero-gradients of the previous experiment.

8.5. Comparison of Self-Attention with Soft Attention as implemented in DuPLO

In the previous experiment, we explored the self-attention mechanism, as implemented in cascaded layers of the transformer model. The DuPLO model[59], as described in Section 4.5, proposes a neural network architecture that combines convolutional layers, recurrent layers and a soft-attention mechanism and has been employed for crop type mapping in remote sensing. In Table 1, observed that the duplo architecture achieved good accuracies on preprocessed data, but was outperformed by a purely recurrent model and the self-attention model on the raw time series data. This yields the question of the effectiveness of soft-attention (Section 3.5) compared to self-attention (Section 3.4) which we address in this experiment.

In Fig. 8, we draw the attention scores from two test samples shown in the top row. In the second row, we see the average self-attention scores $\alpha = \frac{1}{T_{out}} \sum_{i=0}^{T_{out}} \mathbf{A}_i$ from the three attention heads of the first transformer layer per input time. This corresponds to the average over the columns in Figs. 7a and 7c. The third row shows the soft-attention scores, as obtained from the duplo model.

Comparing the attention scores, we observe that, consistent with the previous experiment, the self-attention scores focus on few single time instance that obtain classification-relevant features. In contrast, the comparatively simpler soft-attention is not able to focus on single time instances so that multiple neighboring time instances have attention scores greater than zero. Note that the soft-attention scores are calculated within the recurrent branch of the Duplo model that uses a complex combination of convolutional layers combined with a single mono-directional recurrent layer. The limitations of these attention scores may be also caused by the preceding layers. For instance, the mono-directional encoding of the gated recurrent unit of the duplo model likely leads to higher-level features in the latter half of the time series. It is likely that this effect causes the higher attention scores focusing on the later time instances where more expressive recurrent features have been extracted from the single mono-directional GRU layer.

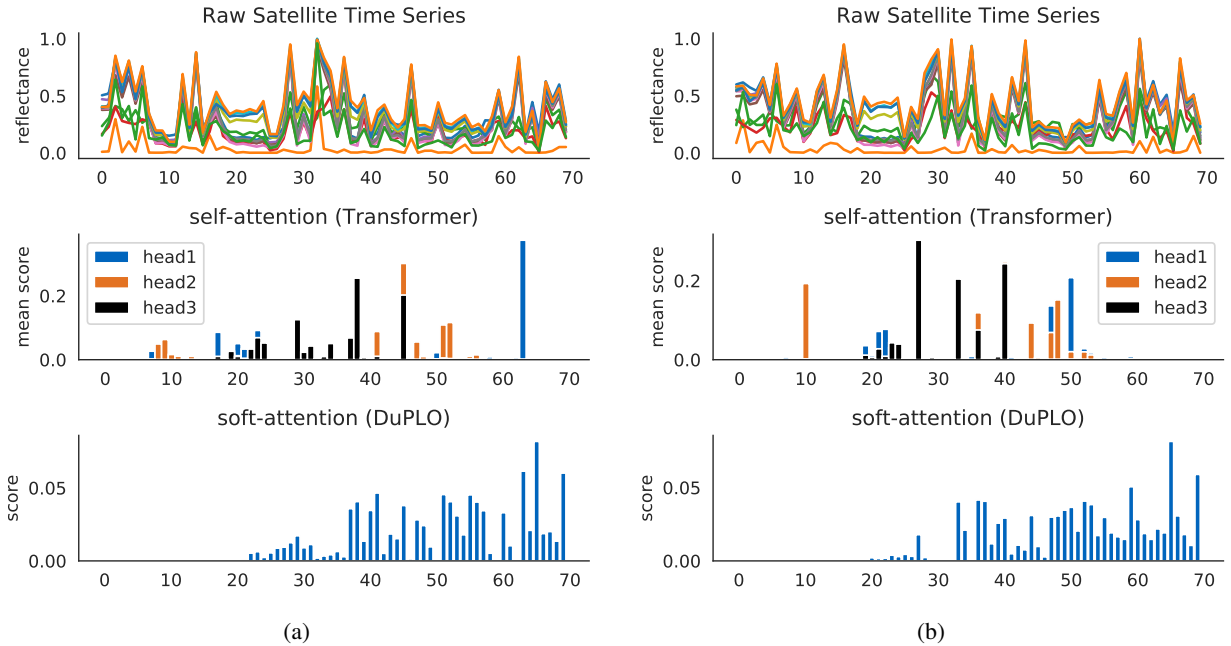


Figure 8: Comparison of self-attention scores, as implemented in the transformer model, with soft-attention scores used in the DuPLO model

Overall, we conclude that the self-attention mechanism can be, by its design with three dense layers, more expressive than the simpler soft-attention that requires only one dense layer. However, the architecture of the DuPLO model, that comprises a mixture of convolutional, recurrent, and attention layers, makes it difficult to isolate the effects of the individual layers in comparison to the other model architectures that exclusively rely on one type of layer architecture.

8.6. Feature Separability Analyses through Manifold Embeddings

Deep learning models, in general, extract features of increasingly complexity throughout the cascaded layer architectures [91]. In this experiment, we analyzed this property by visualizing the hidden features at varying deeper layers of the transformer architecture, as shown in Fig. 9. For this analysis, we extract $D = 128$ -dimensional feature vectors after encoding time series samples from the test-dataset. We project them into a two-dimensional embedding space via *t-distributed stochastic neighbor embedding (t-SNE)* [92], *Uniform manifold approximation and projection (UMAP)* [93], as used in [94], and *Principal Component Analysis (PCA)*. We used a trained transformer network with three self-attention layers and $D = 128$ hidden dimensions. To obtain the features, we passed the entire test dataset over all regions through a pre-trained transformer network and recorded the hidden features after each self-attention layer and after the last dense layer before max pooling and softmax activation, as visualized in Fig. 9. The original features $\mathbf{H} \in \mathbb{R}^{(T=70) \times (D=128)}$ were then averaged along the time dimension to obtain $\mathbf{h}' \in \mathbb{R}^{D=128}$ and mapped into the final embedding space $\mathbb{R}^{D=2}$. The illustration shows the representations of the embedded 200 samples for each of the 23 land use classes. We augmented the final plots with a key indicating the classes identities and a schematic picture of the network topology. Since the class definitions are rather broad with, for instance, multiple categories of grassland, we grouped them by color but assigned varying marker shapes to each class. Note, that the embeddings rely on the extracted features without taking the actual ground truth class label into account. One can easily observe that the transformed features become more and more separable with each deeper network layer throughout all embedding techniques. This becomes apparent by the formation clusters throughout the layers. Looking at the last layer, which is closest to the final prediction, we can identify distinct separable manifolds for corn (★) and rapeseed (★). This suggests that these classes are well-separable in the feature space. This observation is clearly observable for both the

non-linear T-SNE and UMAP projections while the separability in the first two principle components in the linear PCA projection is less pronounced.

From expert knowledge provided by the *Bavarian Ministry of Agriculture*, we account for a certain degree of wrong labels in the dataset. The identification of these outliers is a key motivation for crop type monitoring. Hence, these few field parcels may have been assigned wrong labels by the respective farmer.

In summary, the feature extraction capabilities learned by this self-attention network is consistent with assumptions based on domain-knowledge of the particular classes. Methodologically, we observed that features from deeper cascaded network layers get increasingly distinctive and field parcels of the same label are mapped in similar embedded regions. We would like to stress that this type of analysis is not unique to self-attention networks and can be reproduced for many deep learning architectures that extracts features in cascaded layers.

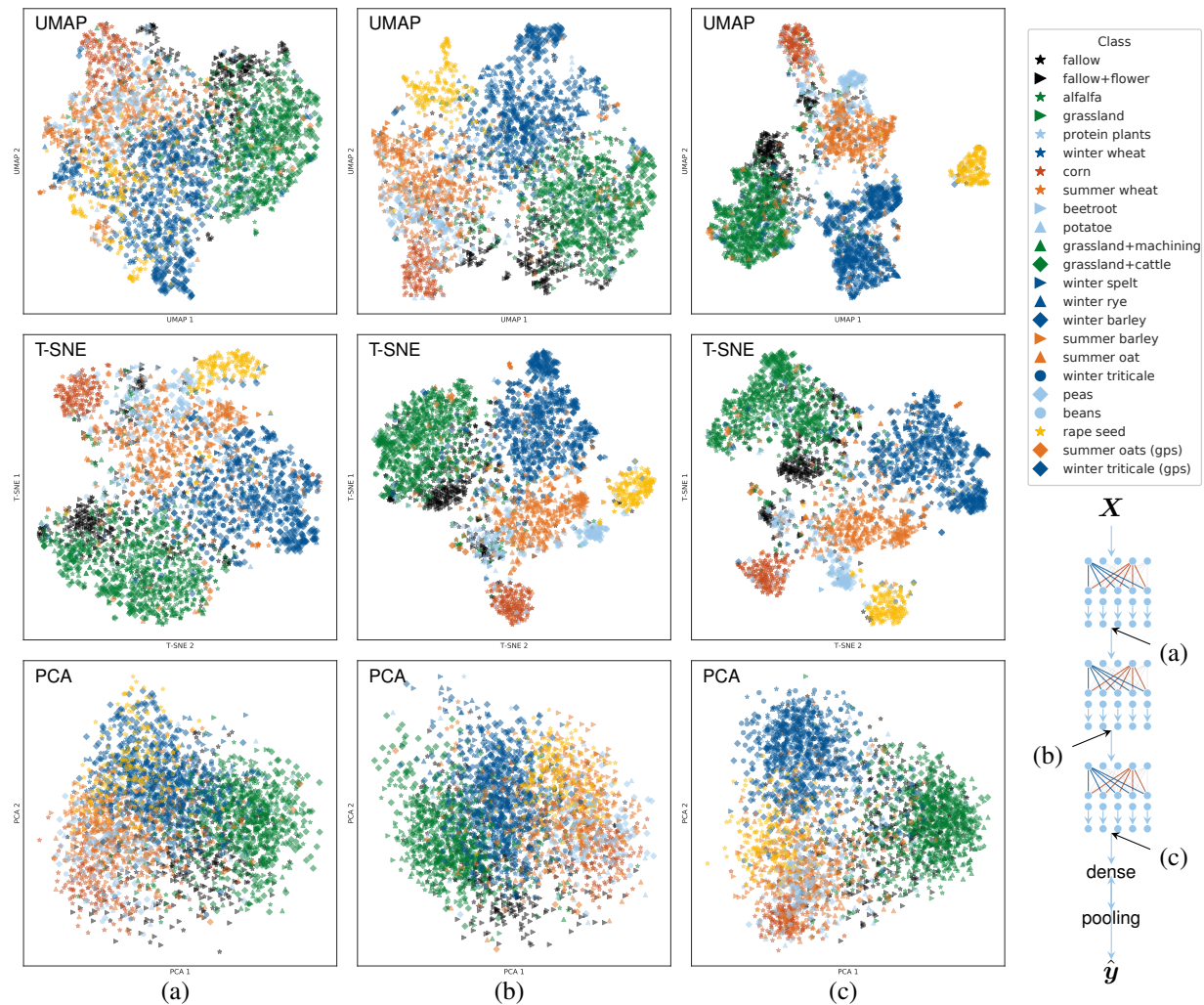


Figure 9: Feature embedding at varying depths of the Transformer Network. Each self-attention layer increases separability of the extracted features.

9. Conclusion

In this work, we quantitatively and qualitatively analyzed self-attention for the application in multi-temporal Earth observation. We performed a large-scale quantitative comparison in Section 8.1 where we evaluated multiple model

architectures that rely on self-attention, recurrence and convolution, and a random forest baseline. We compared these models from multiple angles by reporting their performance on preprocessed and raw Sentinel 2 time series as well as land-use and a land-cover oriented set of classes. Here, we observed that all models performed equally well on preprocessed data. Even the random forest baseline achieved competitive overall accuracy. This leads to the conclusion that the choice of model architecture is less critical when extensive data preprocessing is utilized as a form of feature extraction aided by region-specific expert knowledge. For raw unprocessed Sentinel 2 time series data, the Transformer, and LSTM-RNN architectures were able to achieve better accuracies compared to the convolutional models. We investigated this further by a feature importance analysis in Section 8.3 using gradients where we observed that the mechanisms self-attention and recurrence helped to suppress information not relevant for classification in the time series. For the Transformer, this was realized by learning weights in the attention mechanism which enables the model to specifically focus on some observations, as could be observed in Fig. 1 in Section 8.4. Finally, we looked at the larger Transformer network topology and observed how deeper neural network layers were able to learn increasingly separable representations of the classes in Section 8.6. Since we chose a challenging set of classes, class overlaps in the semantic representation of classes with common properties were present and followed common intuition. This is a typical challenge for land cover and land use classification with long-tailed class distributions.

To summarize, we saw that self-attention is a promising technique that allows neural networks to extract features from specific time instances with raw optical satellite time series. It suits well in the canon of time series classification models that utilize recurrent or convolutional layers. We did not find any mechanism among the compared baseline methods that systematically achieved better accuracies, but observed that self-attention and recurrence were, by design of the feature extraction, more robust to noise in the data and could better suppress cloudy observations in raw time series.

In the future, a robust classification of raw time series data without region-specific expert knowledge will be key to quantitatively exploit the satellite data that is published daily. We hope to have contributed a step towards this direction by this comprehensive study that evaluated model accuracies on preprocessed and raw data for a variety of mechanisms for time series classification.

10. Acknowledgements

We would like to thank Sabine Erbe from the Bavarian Ministry of Agriculture for the continuous and persistent support and valuable domain knowledge as well as Markus Ziegler and Christoph Schmidt from GAF-AG for their collaboration in the joint crop type classification project which provided objective, method and preprocessed time series data for this study. The work of Marc Rußwurm was funded by the *German Federal Ministry for Economic Affairs and Energy (BMWi)* under reference *50EE1908*.

References

- [1] C. E. Woodcock, R. Allen, M. Anderson, A. Belward, R. Bindschadler, W. Cohen, F. Gao, S. N. Goward, D. Helder, E. Helmer, et al., Free access to landsat imagery, *Science* 320 (5879) (2008) 1011–1011.
- [2] M. A. Wulder, T. R. Loveland, D. P. Roy, C. J. Crawford, J. G. Masek, C. E. Woodcock, R. G. Allen, M. C. Anderson, A. S. Belward, W. B. Cohen, et al., Current status of landsat program, science, and applications, *Remote sensing of environment* 225 (2019) 127–147.
- [3] B. C. Reed, J. F. Brown, D. VanderZee, T. R. Loveland, J. W. Merchant, D. O. Ohlen, Measuring Phenological Variability from Satellite Imagery, *Journal of Vegetation Science* 5 (5) (1994) 703–714. doi:10.2307/3235884.
- [4] J. B. Odenweller, K. I. Johnson, Crop identification using Landsat temporal-spectral profiles, *Remote Sensing of Environment* 14 (1-3) (1984) 39–5. doi:10.1016/0034-4257(84)90006-3.
- [5] M. A. Wulder, W. A. Kurz, M. Gillis, et al., National level forest monitoring and modeling in Canada, *Progress in Planning* 61 (4) (2004) 365–381.
- [6] M. Herold, S. Carter, V. Avitabile, A. B. Espejo, I. Jonckheere, R. Lucas, R. E. McRoberts, E. Næsset, J. Nightingale, R. Petersen, et al., The role and need for space-based forest biomass-related measurements in environmental management and policy, *Surveys in Geophysics* 40 (4) (2019) 757–778.
- [7] J. Reiche, R. Lucas, A. L. Mitchell, J. Verbesselt, D. H. Hoekman, J. Haarpaintner, J. M. Kellndorfer, A. Rosenqvist, E. A. Lehmann, C. E. Woodcock, et al., Combining satellite data for better tropical forest monitoring, *Nature Climate Change* 6 (2016) 120–122.
- [8] Sentinel data access annual report 2019, date 06/05/19, COPE-SERCO-RP-19-0389 (2019).
- [9] S. Foerster, K. Kaden, M. Foerster, S. Itzerott, Crop type mapping using spectral-temporal profiles and phenological information, *Computers and Electronics in Agriculture* 89 (2012) 30–40. doi:10.1016/j.compag.2012.07.015.
- [10] C. Conrad, S. Fritsch, J. Zeidler, G. Rücker, S. Dech, Per-Field Irrigated Crop Classification in Arid Central Asia Using SPOT and ASTER Data, *Remote Sensing* 2 (4) (2010) 1035–1056. doi:10.3390/rs2041035.

- [11] C. Conrad, S. Dech, O. Dubovyk, S. Fritsch, D. Klein, F. Löw, G. Schorcht, J. Zeidler, Derivation of temporal windows for accurate crop discrimination in heterogeneous croplands of Uzbekistan using multitemporal RapidEye images, *Computers and Electronics in Agriculture* 103 (2014) 63–74. doi:10.1016/j.compag.2014.02.003.
- [12] P. Hao, Y. Zhan, L. Wang, Z. Niu, M. Shakir, Feature Selection of Time Series MODIS Data for Early Crop Classification Using Random Forest: A Case Study in Kansas, USA, *Remote Sensing* 7 (5) (2015) 5347–5369. doi:10.3390/rs70505347.
- [13] J. M. Peña-Barragán, M. K. Ngugi, R. E. Plant, J. Six, Object-based crop identification using multiple vegetation indices, textural features and crop phenology, *Remote Sensing of Environment* 115 (6) (2011) 1301–1316. doi:10.1016/j.rse.2011.01.009.
- [14] L. Zhong, L. Hu, H. Zhou, Deep learning based multi-temporal crop classification, *Remote sensing of environment* 221 (2019) 430–443.
- [15] S. Valero, D. Morin, J. Inglada, G. Sepulcre, M. Arias, O. Hagolle, G. Dedieu, S. Bontemps, P. Defourny, B. Koetz, Production of a dynamic cropland mask by processing remote sensing image series at high temporal and spatial resolutions, *Remote Sensing* 8 (1) (2016) 1–21. doi:10.3390/rs8010055.
- [16] P. Kumar, D. K. Gupta, V. N. Mishra, R. Prasad, Comparison of support vector machine, artificial neural network, and spectral angle mapper algorithms for crop classification using LISS IV data, *International Journal of Remote Sensing* 36 (6) (2015) 1604–1617. doi:10.1080/2150704X.2015.1019015.
- [17] B. Zheng, S. W. Myint, P. S. Thenkabail, R. M. Aggarwal, A support vector machine to identify irrigated crop types using time-series landsat ndvi data, *International Journal of Applied Earth Observation and Geoinformation* 34 (2015) 103–112.
- [18] R. Devadas, R. Denham, M. Pringle, Support vector machine classification of object-based data for crop mapping, using multi-temporal landsat imagery, *Int. Arch. Photogramm. Remote Sens. Spat. Inf. Sci* 39 (2012) 185–190.
- [19] C. Ünsalan, K. L. Boyer, Review on Land Use Classification, in: *Multispectral Satellite Image Understanding: From Land Classification to Building and Road Detection*, Springer, 2011, pp. 49–64. doi:10.1007/978-0-85729-667-2_5.
- [20] Y. Shao, R. S. Lunetta, Comparison of support vector machine, neural network, and cart algorithms for the land-cover classification using limited training data points, *ISPRS Journal of Photogrammetry and Remote Sensing* 70 (2012) 78–87.
- [21] P. Jönsson, L. Eklundh, Timesat—a program for analyzing time-series of satellite sensor data, *Computers & Geosciences* 30 (8) (2004) 833–845.
- [22] L. Eklundh, P. Jönsson, Timesat for processing time-series data from satellite sensors for land surface monitoring, in: *Multitemporal Remote Sensing*, Springer, 2016, pp. 177–194.
- [23] M. A. White, K. M. de Beurs, K. Didan, D. W. Inouye, A. D. Richardson, O. P. Jensen, J. O’KEEFE, G. Zhang, R. R. Nemani, W. J. van Leeuwen, et al., Intercomparison, interpretation, and assessment of spring phenology in north america estimated from remote sensing for 1982–2006, *Global Change Biology* 15 (10) (2009) 2335–2359.
- [24] L. Olsson, L. Eklundh, J. Ardö, A recent greening of the sahel—trends, patterns and potential causes, *Journal of Arid Environments* 63 (3) (2005) 556–566.
- [25] K. Jia, S. Liang, X. Wei, Y. Yao, Y. Su, B. Jiang, X. Wang, Land cover classification of landsat data with phenological features extracted from time series modis ndvi data, *Remote sensing* 6 (11) (2014) 11518–11532.
- [26] M. Singha, B. Wu, M. Zhang, An object-based paddy rice classification using multi-spectral data and crop phenology in assam, northeast india, *Remote Sensing* 8 (6) (2016) 479.
- [27] Z. Zhu, C. E. Woodcock, Continuous change detection and classification of land cover using all available landsat data, *Remote sensing of Environment* 144 (2014) 152–171.
- [28] Z. Zhu, C. E. Woodcock, Object-based cloud and cloud shadow detection in landsat imagery, *Remote sensing of environment* 118 (2012) 83–94.
- [29] Z. Zhu, S. Wang, C. E. Woodcock, Improvement and expansion of the fmask algorithm: Cloud, cloud shadow, and snow detection for landsats 4–7, 8, and sentinel 2 images, *Remote Sensing of Environment* 159 (2015) 269–277.
- [30] J. O. Street, R. J. Carroll, D. Ruppert, A note on computing robust regression estimates via iteratively reweighted least squares, *The American Statistician* 42 (2) (1988) 152–154.
- [31] W. Dumouchel, F. O’Brien, et al., Integrating a robust option into a multiple regression computing environment, in: *Computer science and statistics: Proceedings of the 21st symposium on the interface*, American Statistical Association Alexandria, VA, 1989, pp. 297–302.
- [32] J. Verbesselt, R. Hyndman, G. Newnham, D. Culvenor, Detecting trend and seasonal changes in satellite image time series, *Remote sensing of Environment* 114 (1) (2010) 106–115.
- [33] R. E. Kennedy, Z. Yang, W. B. Cohen, Detecting trends in forest disturbance and recovery using yearly landsat time series: 1. landtrendr—temporal segmentation algorithms, *Remote Sensing of Environment* 114 (12) (2010) 2897–2910.
- [34] W. S. McCulloch, W. Pitts, A logical calculus of the ideas immanent in nervous activity, *The bulletin of mathematical biophysics* 5 (4) (1943) 115–133.
- [35] J. D. Cowan, Neural networks: the early days, in: *Advances in neural information processing systems*, 1990, pp. 828–842.
- [36] Y. LeCun, L. Bottou, Y. Bengio, P. Haffner, et al., Gradient-based learning applied to document recognition, *Proceedings of the IEEE* 86 (11) (1998) 2278–2324.
- [37] J. Deng, W. Dong, R. Socher, L.-J. Li, K. Li, L. Fei-Fei, Imagenet: A large-scale hierarchical image database, in: *2009 IEEE conference on computer vision and pattern recognition*, IEEE, 2009, pp. 248–255.
- [38] O. Russakovsky, J. Deng, H. Su, J. Krause, S. Satheesh, S. Ma, Z. Huang, A. Karpathy, A. Khosla, M. Bernstein, et al., Imagenet large scale visual recognition challenge, *International journal of computer vision* 115 (3) (2015) 211–252.
- [39] K. Simonyan, A. Zisserman, Very deep convolutional networks for large-scale image recognition, *arXiv preprint arXiv:1409.1556v6*.
- [40] A. Krizhevsky, I. Sutskever, G. E. Hinton, Imagenet classification with deep convolutional neural networks, in: *Advances in neural information processing systems*, 2012, pp. 1097–1105.
- [41] K. He, X. Zhang, S. Ren, J. Sun, Deep residual learning for image recognition, in: *Proceedings of the IEEE conference on computer vision and pattern recognition*, 2016, pp. 770–778.
- [42] J. Long, E. Shelhamer, T. Darrell, Fully convolutional networks for semantic segmentation, in: *Proceedings of the IEEE conference on computer vision and pattern recognition*, 2015, pp. 3431–3440.

- [43] C. Szegedy, S. Ioffe, V. Vanhoucke, A. A. Alemi, Inception-v4, inception-resnet and the impact of residual connections on learning, in: Thirty-First AAAI Conference on Artificial Intelligence, 2017.
- [44] A. Vaswani, N. Shazeer, N. Parmar, J. Uszkoreit, L. Jones, A. N. Gomez, Ł. Kaiser, I. Polosukhin, Attention is all you need, in: Advances in neural information processing systems, 2017, pp. 5998–6008.
- [45] J. Devlin, M.-W. Chang, K. Lee, K. Toutanova, Bert: Pre-training of deep bidirectional transformers for language understanding, arXiv preprint arXiv:1810.04805v2.
- [46] A. Radford, J. Wu, R. Child, D. Luan, D. Amodei, I. Sutskever, Language models are unsupervised multitask learners, OpenAI Blog 1 (8).
- [47] D. Marmanis, M. Datcu, T. Esch, U. Stilla, Deep learning earth observation classification using imagenet pretrained networks, IEEE Geoscience and Remote Sensing Letters 13 (1) (2015) 105–109.
- [48] M. Volpi, D. Tuia, Dense semantic labeling of subdecimeter resolution images with convolutional neural networks, IEEE Transactions on Geoscience and Remote Sensing 55 (2) (2016) 881–893.
- [49] J. Sherrah, Fully convolutional networks for dense semantic labelling of high-resolution aerial imagery, arXiv preprint arXiv:1606.02585v1.
- [50] N. Audebert, B. Le Saux, S. Lefèvre, Semantic segmentation of earth observation data using multimodal and multi-scale deep networks, in: Asian conference on computer vision, Springer, 2016, pp. 180–196, v1.
- [51] G. Cheng, P. Zhou, J. Han, Learning rotation-invariant convolutional neural networks for object detection in vhr optical remote sensing images, IEEE Transactions on Geoscience and Remote Sensing 54 (12) (2016) 7405–7415.
- [52] G. Cheng, J. Han, X. Lu, Remote sensing image scene classification: Benchmark and state of the art, Proceedings of the IEEE 105 (10) (2017) 1865–1883.
- [53] G. Cheng, C. Yang, X. Yao, L. Guo, J. Han, When deep learning meets metric learning: Remote sensing image scene classification via learning discriminative cnns, IEEE Transactions on Geoscience and Remote Sensing 56 (5) (2018) 2811–2821.
- [54] M. Rußwurm, M. Körner, Temporal vegetation modelling using long short-term memory networks for crop identification from medium-resolution multi-spectral satellite images, in: Proceedings of the IEEE Conference on Computer Vision and Pattern Recognition Workshops, 2017, pp. 11–19.
- [55] X. Jia, A. Khandelwal, G. Nayak, J. Gerber, K. Carlson, P. West, V. Kumar, Incremental Dual-memory LSTM in Land Cover Prediction, in: 23rd ACM SIGKDD International Conference on Knowledge Discovery and Data Mining, 2017, pp. 867–876. doi:10.1145/3097983.3098112.
- [56] H. Lyu, H. Lu, L. Mou, Learning a Transferable Change Rule from a Recurrent Neural Network for Land Cover Change Detection, Remote Sensing 8 (12) (2016) 506. doi:10.3390/rs8060506.
- [57] L. Mou, L. Bruzzone, X. X. Zhu, Learning spectral-spatial-temporal features via a recurrent convolutional neural network for change detection in multispectral imagery, IEEE Transactions on Geoscience and Remote Sensing 57 (2) (2018) 924–935.
- [58] P. Benedetti, D. Ienco, R. Gaetano, K. Ose, R. G. Pensa, S. Dupuy, M3fusion: A deep learning architecture for multiscale multimodal multitemporal satellite data fusion, IEEE Journal of Selected Topics in Applied Earth Observations and Remote Sensing 11 (12) (2018) 4939–4949.
- [59] R. Interdonato, D. Ienco, R. Gaetano, K. Ose, DuPLO: A DUAL view Point deep Learning architecture for time series classificatiOn, ISPRS Journal of Photogrammetry and Remote Sensing 149 (2019) 91–104. doi:10.1016/j.isprsjprs.2019.01.011.
- [60] P. J. Werbos, Backpropagation through time: what it does and how to do it, Proceedings of the IEEE 78 (10) (1990) 1550–1560.
- [61] S. Hochreiter, J. Schmidhuber, Long Short-Term Memory, Neural Computation 9 (8) (1997) 1735–1780. doi:10.1162/neco.1997.9.8.1735.
- [62] J. Chung, C. Gulcehre, K. Cho, Y. Bengio, Empirical evaluation of gated recurrent neural networks on sequence modeling, arXiv preprint arXiv:1412.3555v1.
- [63] I. Sutskever, O. Vinyals, Q. V. Le, Sequence to sequence learning with neural networks, in: Advances in neural information processing systems, 2014, pp. 3104–3112.
- [64] V. S. F. Garnot, L. Landrieu, S. Giordano, N. Chehata, Time-Space Tradeoff in Deep Learning Models for Crop Classification on Satellite Multi-Spectral Image Time Series, in: IEEE International Geoscience and Remote Sensing Symposium (IGARSS), 2019, pp. 6247–6250. doi:10.1109/IGARSS.2019.8900517.
- [65] A. Sharma, X. Liu, X. Yang, Land cover classification from multi-temporal, multi-spectral remotely sensed imagery using patch-based recurrent neural networks, Neural Networks 105 (2018) 346–355.
- [66] M. Rußwurm, M. Körner, Multi-temporal land cover classification with sequential recurrent encoders, ISPRS International Journal of Geo-Information 7 (4) (2018) 129.
- [67] D. Bahdanau, J. Chorowski, D. Serdyuk, P. Brakel, Y. Bengio, End-to-end attention-based large vocabulary speech recognition, in: 2016 IEEE international conference on acoustics, speech and signal processing (ICASSP), IEEE, 2016, pp. 4945–4949.
- [68] H. I. Fawaz, G. Forestier, J. Weber, L. Idoumghar, P.-A. Muller, Deep learning for time series classification: a review, Data Mining and Knowledge Discovery 33 (4) (2019) 917–963.
- [69] C. Pelletier, G. I. Webb, F. Petitjean, Temporal convolutional neural network for the classification of satellite image time series, Remote Sensing 11 (5) (2019) 523.
- [70] V. S. F. Garnot, L. Landrieu, S. Giordano, N. Chehata, Satellite Image Time Series Classification with Pixel-Set Encoders and Temporal Self-Attention, arXiv e-printsV1. arXiv:1911.07757.
- [71] D. E. Rumelhart, G. E. Hinton, R. J. Williams, Learning representations by back-propagating errors, Nature 323 (6088) (1986) 533–536. doi:10.1038/323533a0.
- [72] R. Jozefowicz, W. Zaremba, I. Sutskever, An Empirical Exploration of Recurrent Network Architectures, in: Proceedings of the 32nd International Conference on Machine Learning (ICML), Proceedings of Machine Learning Research, 2015, pp. 2342–2350.
- [73] B. Yoshua, S. Patrice, F. Paolo, Learning long-term dependencies with gradient descent is difficult, IEEE transactions on neural networks 5 (2) (1994) 157–166.
- [74] H. Ismail Fawaz, B. Lucas, G. Forestier, C. Pelletier, D. F. Schmidt, J. Weber, G. I. Webb, L. Idoumghar, P.-A. Muller, F. Petitjean, Inception-time: Finding alexnet for time series classification, ArXivV1.

- [75] N. Hatami, Y. Gavet, J. Debayle, Classification of time-series images using deep convolutional neural networks, in: Tenth International Conference on Machine Vision (ICMV 2017), Vol. 10696, International Society for Optics and Photonics, 2018, p. 106960Y.
- [76] D. Britz, M. Y. Guan, M.-T. Luong, Efficient attention using a fixed-size memory representation, arXiv preprint arXiv:1707.00110V1.
- [77] S. Ioffe, C. Szegedy, Batch normalization: Accelerating deep network training by reducing internal covariate shiftV3. arXiv:1502.03167v3.
- [78] Z. Wang, W. Yan, T. Oates, Time series classification from scratch with deep neural networks: A strong baseline, in: 2017 international joint conference on neural networks (IJCNN), IEEE, 2017, pp. 1578–1585.
- [79] Z. Cui, W. Chen, Y. Chen, Multi-scale convolutional neural networks for time series classification, arXiv preprint arXiv:1603.06995V4.
- [80] H. A. Dau, A. Bagnall, K. Kamgar, C.-C. M. Yeh, Y. Zhu, S. Gharghabi, C. A. Ratanamahatana, E. Keogh, The ucr time series archive, arXiv preprint arXiv:1810.07758V2.
- [81] A. Bagnall, H. A. Dau, J. Lines, M. Flynn, J. Large, A. Bostrom, P. Southam, E. Keogh, The uea multivariate time series classification archive, 2018, arXiv preprint arXiv:1811.00075V1.
- [82] F. Pedregosa, G. Varoquaux, A. Gramfort, V. Michel, B. Thirion, O. Grisel, M. Blondel, P. Prettenhofer, R. Weiss, V. Dubourg, et al., Scikit-learn: Machine learning in python, *Journal of machine learning research* 12 (Oct) (2011) 2825–2830.
- [83] D. P. Kingma, J. Ba, Adam: A method for stochastic optimization, arXiv preprint arXiv:1412.6980V9.
- [84] J. Cohen, A coefficient of agreement for nominal scales, *Educational and Psychological Measurement* 20 (1960) 37–46.
- [85] J. Bergstra, D. Yamins, D. D. Cox, Hyperopt: A python library for optimizing the hyperparameters of machine learning algorithms, in: *Proceedings of the 12th Python in science conference*, Citeseer, 2013, pp. 13–20.
- [86] L. Li, K. Jamieson, A. Rostamizadeh, E. Gonina, M. Hardt, B. Recht, A. Talwalkar, Massively parallel hyperparameter tuning, arXiv preprint arXiv:1810.05934V5.
- [87] R. Liaw, E. Liang, R. Nishihara, P. Moritz, J. E. Gonzalez, I. Stoica, Tune: A research platform for distributed model selection and training, arXiv preprint arXiv:1807.05118V1.
- [88] P. Schratz, J. Muenchow, E. Iturritxa, J. Richter, A. Brenning, Performance evaluation and hyperparameter tuning of statistical and machine-learning models using spatial data, arXiv preprint arXiv:1803.11266V1.
- [89] A. Brenning, Spatial cross-validation and bootstrap for the assessment of prediction rules in remote sensing: The r package sperrorest, in: *2012 IEEE international geoscience and remote sensing symposium*, IEEE, 2012, pp. 5372–5375.
- [90] N. Gorelick, M. Hancher, M. Dixon, S. Ilyushchenko, D. Thau, R. Moore, Google earth engine: Planetary-scale geospatial analysis for everyone, *Remote Sensing of Environment* 202 (2017) 18–27.
- [91] I. Goodfellow, Y. Bengio, A. Courville, *Deep learning*, MIT press, 2016.
- [92] L. v. d. Maaten, G. Hinton, Visualizing data using t-sne, *Journal of machine learning research* 9 (Nov) (2008) 2579–2605.
- [93] L. McInnes, J. Healy, J. Melville, Umap: Uniform manifold approximation and projection for dimension reduction, arXiv preprint arXiv:1802.03426V2.
- [94] F. Mohammadimanesh, B. Salehi, M. Mahdianpari, E. Gill, M. Molinier, A new fully convolutional neural network for semantic segmentation of polarimetric sar imagery in complex land cover ecosystem, *ISPRS journal of photogrammetry and remote sensing* 151 (2019) 223–236.